

# The Enrichment of the Intergalactic Medium With Adiabatic Feedback I: Metal Cooling and Metal Diffusion

S. Shen,<sup>1\*</sup> J. Wadsley<sup>1</sup> and G. Stinson<sup>1,2</sup>

<sup>1</sup> *Department of Physics and Astronomy, McMaster University, Main Street West, Hamilton L8S 4M1, Canada*

<sup>2</sup> *Jeremiah Horrocks Institute, University of Central Lancashire, Preston, PR1 2HE*

2 June 2010

## ABSTRACT

A study of metal enrichment of the intergalactic medium (IGM) using a series of smooth particle hydrodynamics (SPH) simulations is presented, employing models for metal cooling and the turbulent diffusion of metals and thermal energy. An adiabatic feedback mechanism was adopted where gas cooling was prevented on the timescale of supernova bubble expansion to generate galactic winds without explicit wind particles. The simulations produced a cosmic star formation history (SFH) that is broadly consistent with observations until  $z \sim 0.5$ , and a steady evolution of the universal neutral hydrogen fraction ( $\Omega_{\text{HI}}$ ) that compares reasonably well with observations. The evolution of the mass and metallicities in stars and various gas phases was investigated. At  $z=0$ , about 40% of the baryons are in the warm-hot intergalactic medium (WHIM), but most metals (80%-90%) are locked in stars. At higher redshifts the proportion of metals in the IGM is higher due to more efficient loss from galaxies. The results also indicate that IGM metals primarily reside in the WHIM throughout cosmic history, which differs from simulations with hydrodynamically decoupled explicit winds. The metallicity of the WHIM lies between 0.01 and 0.1 solar with a slight decrease at lower redshifts. The metallicity evolution of the gas inside galaxies are broadly consistent with observations, but the diffuse IGM is under enriched at  $z \sim 2.5$ .

Galactic winds most efficiently enrich the IGM for halos in the intermediate mass range  $10^{10}M_{\odot} - 10^{11} M_{\odot}$ . At the low mass end gas is prevented from accreting onto halos and has very low metallicities. At the high mass end, the fraction of halo baryons escaped as winds declines along with the decline of stellar mass fraction of the galaxies. This is likely because of the decrease in star formation activity and decrease in wind escape efficiency. Metals enhance cooling which allows WHIM gas to cool onto galaxies and increases star formation. Metal diffusion allows winds to mix prior to escape, decreasing the IGM metal content in favour of gas within galactic halos and star forming gas. Diffusion significantly increases the amount of gas with low metallicities and changes the density-metallicity relation.

## 1 INTRODUCTION

The intergalactic medium (IGM) contains most of the baryons in the Universe and it provides the fuel for galaxies to form stars in which metals are produced. In turn, supernovae and galactic winds enrich the IGM with metals, while stars and active galactic nuclei (AGN) emit UV photons. This interplay between the IGM and galaxies, mediated by metal cooling in the presence of UV, regulates the formation of stars in the universe. The evolution and enrichment history of the IGM provides a record of this interplay.

Observations of metal absorption lines (e.g., C III, C IV, Si III, S IV and O VI) in quasar spectra show that the intergalactic medium (IGM) far outside large galaxies ( $\rho/\rho_{\text{mean}} < 10$ ) is enriched (e.g. Songaila & Cowie 1996; Davé et al. 1998; Ellison et al. 2000; Schaye et al. 2000; Pettini et al. 2003; Schaye et al. 2003; Aguirre et al. 2004;

Simcoe et al. 2004). There is evidence for enrichment extending back to  $z > 5$  (Pettini et al. 2003; Simcoe 2006) though metallicities do not evolve much from  $z=4$  to  $z=2$  (Schaye et al. 2003). Since metals are created in stars inside galaxies, those in the IGM must have escaped from galaxies. Exactly how this occurs is unclear. It typically assumed that galactic winds, driven by star formation, dominate IGM enrichment (Aguirre & Schaye 2007). Winds can be either launched as the ejecta of a large number of co-existing supernova (SN) explosions (Heckman et al. 1990), driven by the injection of momentum by SN and stellar winds or by radiation pressure from starbursts and AGN (Murray et al. 2005). Observations of galactic winds (e.g., Heckman 2001; Pettini et al. 2001) have found that galactic wind velocities range from hundreds to thousands of km/s and the mass loss rates are comparable to star formation rates. Wind material has a complex, multiphase structure but most metals are

expected to be entrained in the hot phase (Veilleux et al. 2005, and references therein).

Although detailed hydrodynamical simulations of the interstellar medium (ISM) in galaxies (e.g., Mac Low & Ferrara 1999; Strickland & Stevens 2000; Williams & Dyson 2002) have been able to generate galactic outflows and have explored various properties of winds and the gas dynamics in different phases, current cosmological simulations lack the resolution to launch or track winds directly. Hot, low density SN bubbles are unresolved in such simulations which initially led to an overcooling problem that produced unrealistically concentrated simulated galaxies (Navarro & Steinmetz 1997). As a result, various “subgrid” stellar feedback and wind models have emerged. These models serve two functions: to regulate star formation and the properties of the ISM and to redistribute gas (and newly formed metals) both within and into the environment around galaxies. There are three main approaches, energetic feedback, kinetic feedback and modifications to the effective equation of state which behaves similarly to an increased effective pressure.

Energetic feedback in its simplest form involves simply adding the stellar feedback as thermal energy, but this suffers from overcooling (Katz et al. 1996). Kinetic feedback (e.g., Navarro & White 1993; Springel & Hernquist 2003; Oppenheimer & Davé 2006; Dalla Vecchia & Schaye 2008) converts part of the SN energy into kinetic energy in the gas. The effectiveness of kinetic feedback is strongly dependent on the resolution and hydrodynamic method.

Springel & Hernquist (2003) argued that regulated star formation creates an effective pressure in the ISM and this was modelled directly in the GADGET code as part of a recipe for regulated star formation. This approach leads to a strongly hydrodynamically-coupled, multiphase ISM that does not naturally produce galactic outflows. To combat this the authors added a “superwind” model where fluid elements in the star forming region are ejected at fixed speed and are also hydrodynamically decoupled until they leaves the galaxy. Oppenheimer & Davé (2006) modified the model in a manner referred to as the momentum-driven wind scenario so that the velocity of the wind and the mass loading factor were related to the velocity dispersion of the host galaxy. The GADGET code with superwind feedback prescriptions has been widely used in various problems such as damped Lyman- $\alpha$  (DLA) absorbers (Nagamine et al. 2004a,b) and the enrichment of the IGM at high and low redshifts (Oppenheimer & Davé 2006, 2009). According to these works, superwind feedback is essential to suppress overproduction of stars in galaxies and to reproduce the cosmic SFH at high redshift. It also increases the local fraction of the warm-hot intergalactic medium (WHIM) to a sufficient percentage (40% to 50%) to account for the “missing baryons” at  $z = 0$ . Although aspects of the model compare well with observations, some components do not. For example, the feedback may eject a large amount of cool gas from the galactic disks, which results in a low neutral hydrogen mass density  $\Omega_{\text{HI}}$  at  $z < 2$  (Nagamine et al. 2004a). Also, the interaction between winds and the ISM is usually not modeled in these simulations. Dalla Vecchia & Schaye (2008) found that the ISM plays an important role in regulating the amount of wind that escapes and the morphology of the galaxies. In their model winds are not hydrodynam-

ically decoupled, which naturally allows for variable mass loading.

A refined version of energetic feedback is adiabatic feedback which treats the overcooling problem by inhibiting gas from cooling until the hot SN bubbles can be resolved (e.g., Thacker & Couchman 2000; Kay et al. 2002; Sommer-Larsen et al. 2003; Stinson et al. 2006). This is the approach used in this work. The pressure of the hot gas accelerates the ISM to generate winds. In the high resolution limit, this method approaches direct ISM modeling. Though energetic feedback is often referred to as supernova feedback, it can be used to model several types of stellar feedback such as winds and locally deposited radiation energy. The essential quantity is the energy injection rate as a function of the mass in stars and the current age of the stellar population.

Theuns et al. (2002) used the Kay et al. (2002) adiabatic feedback model that turned off cooling for 10 Myrs for the feedback gas in their cosmological simulations. They found enough metals were carried by strong winds to produce C IV absorption lines that agreed with observations. Aguirre et al. (2005) used the same simulation to compare the optical depth of C IV and C III absorption lines from simulations with observations.

The properties of the enriched IGM are not only affected by winds but also by gas cooling. Winds can enrich galactic halos and the IGM so that metal cooling significantly increases the cooling rates. Aguirre et al. (2005) found that their simulated metal enriched gas was too hot ( $10^5 \sim 10^7$  K) and suggested that a lack of metal cooling was responsible for discrepancies between simulated and observed C IV absorption. Oppenheimer & Davé (2006) found better agreement when they included the Sutherland & Dopita (1993) metal cooling model. The same model was used by Choi & Nagamine (2009), who investigated the effect of metal cooling on galaxy growth and found that it increases the local star forming efficiency and enhances accretion onto galaxies. However, Sutherland & Dopita (1993) did not include photoionization due to a ultraviolet (UV) radiation background which strongly affects the ionization states of metal species and changes the cooling rates. This is investigated in detail in the current work and also in Wiersma et al. (2009a).

Another important aspect of metal enrichment is the mixing of metals between the wind and the surrounding gas. The interstellar medium is highly turbulent and SN explosions are likely to be a major driver of the turbulence (Mac Low & Klessen 2004). In addition, large velocity shear (such as between a wind and a gaseous halo) naturally generates turbulence and mixing. Turbulent mixing redistributes metals and thermal energy between the wind fluid and the ambient gas. This changes the metallicity, temperature and future evolution of the gas. While metal mixing is expected in strong outflows, it is still unclear how mixing impact the IGM. For example, observations by Schaye et al. (2007) found compact ( $\sim 100$  pc), transient C IV absorbers that are highly enriched, suggesting poor chemical mixing at small scales. These absorbers were interpreted as enriched clumpy medium embedded within hot galactic wind fluids. If velocity shear is the major mechanism for turbulent mixing between winds and the surroundings, then this poor mixing could be explained if the clouds are carried by hot winds at the same speed. However to investigate this in detail,

one must resolve wind structures, which is beyond current cosmological simulations. In this work we will focus on subgrid turbulent mixing models in cosmological context. In SPH simulations (which represent the majority of work in this area), the fluid is modeled by discrete particles. This implies that newly injected metals are locked into specific particles. For example, it was found that the distribution of metals from SPH simulations is too inhomogeneous compared with observations (Aguirre et al. 2005). To assess the potential importance of mixing, Wiersma et al. (2009b) used SPH-smoothed metallicities and compared it with conventional particle metallicities, and found smoothing is able to generate significantly more material with low metallicities. This approach cannot capture the spread of metals over time with its impact on cooling and the thermal history of the gas. Directly modeling the turbulent ISM within a cosmological simulation is far beyond current capabilities. We employed a variant of the Smagorinsky (1963) subgrid turbulent diffusion model, in which unresolved turbulent mixing is treated as a shear-dependent diffusion term. Metal cooling was calculated based on the diffused metals so that its non-local effects could be investigated.

In this work, we present an analysis of a series of SPH cosmological simulations that incorporated adiabatic stellar feedback, detailed metal cooling and turbulent mixing to study the evolution and enrichment of the IGM. The feedback model was kept simple, following the adiabatic stellar feedback approach of Stinson et al. (2006). This model has been calibrated via numerous galaxy formation studies (e.g., Governato et al. 2007). No additional wind prescriptions were used. With this approach, outflows arise from stellar feedback within the ISM and there is no distinction between the feedback that regulates star formation and that which drives galactic outflows. Thus this work establishes a baseline for the effectiveness of moderate stellar feedback coupled with key physical process absent from other work to reproduce the properties of the IGM. These results may be compared with explicit wind models. A further goal of this paper is to separately quantify the impact of metal cooling and turbulent mixing on the SFH, the global properties and the evolution of the IGM and its enrichment. In this first paper of a series, we present general results. The properties of specific metal absorbers in simulated quasar spectra will be presented in a second paper.

This paper is organized as follows. Section 2 describes the models for cosmological hydrodynamics, star formation, supernova feedback, metal cooling and metal diffusion. Section 3 examines the cosmic SFH, global H I fraction and Ly- $\alpha$  decrement in order to calibrate our models. Section 4 focuses on the evolution of the baryonic mass, metal fractions and metallicities in stars and different gas phases. We compare those results to the observed metal fractions and metallicities at different epochs, and with the simulations using different subgrid feedback models from Oppenheimer & Davé (2006), Davé & Oppenheimer (2007) and Wiersma et al. (2009b). In section 5 we analyze the distribution of mass and metallicity in the density-temperature phase diagram at  $z = 0$ . In section 6 we characterize our wind efficiency as a function of galaxy mass to obtain a better understanding of how different phases of the IGM get enriched. Where relevant, we have included detailed analysis of the effects of metal cooling and diffusion, and comparisons with

**Table 1.** List of Simulations

Name	Size (Mpc)	$N_p$	Metal Cooling	Diffusion
mcd_40_256	40.0	$2 \times 256^3$	Yes	Yes
nmc_40_256	40.0	$2 \times 256^3$	No	Yes
nmd_40_256	40.0	$2 \times 256^3$	Yes	No
mcd_45_256	45.6	$2 \times 256^3$	Yes	Yes
mcd_45_512	45.6	$2 \times 512^3$	Yes	Yes

observations. In the final section 7, we summarize and discuss the broader implications.

## 2 METHOD AND SIMULATIONS

Table 1 lists the simulations used in this study. The cosmological parameters are  $(\Omega_m, \Omega_\Lambda, \Omega_b, h, \sigma_8, n) = (0.279, 0.721, 0.0462, 0.701, 0.769, 1.0)$ , consistent with the WMAP 5-year results (Komatsu et al. 2009). The first three simulations in the table share the same initial condition but have different subgrid models for metal cooling and diffusion. The particle mass for gas is  $m_g = 2.4 \times 10^7 M_\odot$  and for dark matter is  $m_d = 1.2 \times 10^8 M_\odot$ . When discussing the effects of metal cooling and diffusion, we will usually refer to the first simulation (mcd\_40\_256) "the reference run". The last two simulations were designed for a convergence study. They have the same initial condition but differ from the first three. The high resolution case has particle masses  $m_d = 3.6 \times 10^7 M_\odot$  and  $m_g = 4.5 \times 10^6 M_\odot$ . All the simulations have the same star formation, metal production and SN feedback models described below. The simulations were run to redshift zero, except for the "mcd\_45\_512" case which was stopped at  $z = 2$ .

The simulations were evolved using the parallel SPH code GASOLINE (Wadsley et al. 2004). GASOLINE solves the equations of hydrodynamics and includes radiative cooling. Gravity is calculated for each particle using a binary tree elements that span at most  $\theta = 0.7$  of the size of the tree element's distance from the particle.

The star formation and feedback recipes used were the "blastwave model" described in detail in Stinson et al. (2006), and they may be summarized as follows. Gas particles must be dense ( $n_{\min} = 0.1 \text{ cm}^{-3}$ ) and cool ( $T_{\max} = 15,000 \text{ K}$ ) to form stars. A subset of the particles that pass these criteria are stochastically selected to form stars based on the commonly used star formation equation,

$$\frac{dM_\star}{dt} = c_\star \frac{M_{gas}}{t_{dyn}} \quad (1)$$

where  $M_\star$  is mass of stars created,  $c_\star$  is a constant star formation efficiency factor,  $M_{gas}$  is the mass of gas creating the star,  $dt$  is how often star formation is calculated (1 Myr in all of the simulations described in this paper) and  $t_{dyn}$  is the gas dynamical time. The constant parameter,  $c_\star$  was set to 0.05 so that a simulated isolated model Milky Way matches the Kennicutt (1998) Schmidt Law (Stinson et al. 2006). Gas particles passing all the criteria form one star. The mass of star formed remains constant throughout the simulation and is set as one-third of the original gas mass ( $8.0 \times 10^6 M_\odot$  for the 40 Mpc,  $256^3$  runs and  $1.5 \times 10^6 M_\odot$  for the  $512^3$  run).

At the resolution of these simulations, each star particle represents a large group of stars. Thus, each particle represents a stellar population covering the entire initial mass function presented in Kroupa et al. (1993). Star masses are converted to stellar lifetimes as described in Raiteri et al. (1996). We implemented feedback from SN II, SN Ia and stellar winds. Metal enrichment from SN II and SN Ia follows the model of Raiteri et al. (1996), but metal production of AGB stars is not included. Stars larger than  $8 M_{\odot}$  explode as SN II during the timestep that overlaps their stellar lifetime after their birth time. The explosion of these stars is treated using the analytic model for blastwaves presented in McKee & Ostriker (1977) as described in detail in Stinson et al. (2006). Gas cooling is suppressed during the expansion of the SN bubble. While the blast radius and the cooling shutoff time are calculated using the full energy output of the supernova, less than half of that energy is transferred to the surrounding ISM,  $E_{SN} = 4 \times 10^{50}$  ergs. The rest of the supernova energy is assumed to be radiated away. The energy is transferred to the ISM by volume weighting (as used in Mashchenko et al. (2008)). Each affected gas particle, with mass  $m_i$  and density  $\rho_i$  receives a fraction of the SN energy and metals proportional to  $m_i W_{ij} / \rho_i$ , where  $W_{ij}$  is the SPH smoothing kernel. A similar method was also adopted in Wiersma et al. (2009b) for the distribution of metals and the energy from SN Ia. The Blastwave model, as currently implemented, has a bias for more cooling suppression at earlier epochs relative to other approaches. Numerical feedback recipes differ substantially from code to code and their results vary with resolution. This provided motivation for the characterization of star formation regulation and wind generation in these simulations that is presented in section 6.

For SN II, metals produced in stars are released as the main sequence progenitors die and distributed to the same gas within the blast radius as is the supernova energy ejected from SN II. Iron and Oxygen are produced in SN II according to the analytic fits used in Raiteri et al. (1996) using the yields from Woosley & Weaver (1995):

$$M_{Fe} = 2.802 \times 10^{-4} M_{\star}^{1.864} \quad (2)$$

$$M_O = 4.586 \times 10^{-4} M_{\star}^{2.721} \quad (3)$$

Feedback from SN Ia also follows the Raiteri et al. (1996) model, as described in detail in Stinson et al. (2006). Radiative cooling was not disabled for SN Ia. Each SN Ia produces  $0.63 M_{\odot}$  Iron and  $0.13 M_{\odot}$  Oxygen (Thielemann et al. 1986) and the metals are ejected into the nearest gas particle for SN Ia. Stellar wind feedback was implemented based on Kennicutt et al. (1994), and the returned mass fraction was determined using a function derived by Weidemann (1987). The returned gas has the same metallicity as the star particle.

## 2.1 Metal Cooling under the UV Radiation

Collisionally excited metal ion species can significantly enhance the cooling of the IGM by their line transitions (see e.g., Sutherland & Dopita (1993)). Metal cooling thus affects the gas temperature, the ionization states of the observable metal species and ultimately the dynamics. It was

not feasible to calculate metal cooling rates during the simulation. Instead, tabulated cooling rates were interpolated during the simulations as in Oppenheimer & Davé (2006), Wiersma et al. (2009b) and Choi & Nagamine (2009). Metal cooling rates were determined from the density, temperature, metallicity of the gas and the radiation background. While the IGM and ISM are exposed to UV radiation, widely-used metal cooling rates (e.g., Sutherland & Dopita 1993; Gnat & Sternberg 2007) were usually calculated assuming collisional ionization equilibrium (CIE), which is only valid when the radiation background is absent. A recent study by Wiersma et al. (2009a) has also investigated the effects of radiation on cooling in the temperature range  $10^4 < T < 10^8$  and also shows that UV largely suppresses the cooling rates and shifts the peaks of the cooling curves to higher temperatures.

The radiative cooling was separated into three components:

$$\Lambda = \Lambda_{H,He} + \Lambda_{metal} + \Lambda_{Comp} \quad (4)$$

where  $\Lambda_{H,He}$  is net cooling due to primordial species (H,  $H^+$ , He,  $He^+$  and  $He^{++}$ ),  $\Lambda_{metal}$  is the rate due to metals, and  $\Lambda_{Comp}$  is the Compton cooling/heating. For the primordial gas the ionization, cooling and heating rates are calculated directly from the ionization equations with rates matching Abel et al. (1997). This enables our simulations to capture the non-equilibrium cooling of primordial species. Although our study focuses mainly on epochs where the IGM is mostly in ionization equilibrium, non-equilibrium effects are important at earlier redshifts, especially during reionization, where temperature changes of several thousand degrees occur as a result of non-equilibrium heating.

We adapted the relation from Jimenez et al. (2003) to estimate the helium mass abundance  $Y$  as it varies with metallicity. For metal mass abundance  $Z < 0.1$ , we assume  $Y = Y_p + (\Delta Y / \Delta Z) Z$ , where  $Y_p = 0.236$  is the helium abundance for primordial gas, and  $\Delta Y / \Delta Z = 2.1$  is the ratio of helium mass to metal mass produced in stars. If the metal mass abundance exceeded 0.1 ( $\sim 10 Z_{\odot}$ ),  $Y$  is linearly decreased so that when  $Z = 1.0$  (100% metals),  $Y = 0$ .

The cooling and heating rates due to metals under the ultraviolet (UV) radiation background were calculated using the photoionization code CLOUDY (version 07.02 Ferland et al. (1998)). CLOUDY output assumes that metals are in ionization equilibrium, a good approximation when extragalactic UV radiation is present. The UV radiation field generally varies its function form in space and time. We assume a uniform background obtained from extracting the CLOUDY (07.02) built-in extragalactic UV background which includes radiation from both quasars and galaxies (Haardt & Madau 2005). The radiation field is a function of wavelength, and it turns on at redshift  $z = 8.9$  and evolves with redshift to  $z=0$ . The same UV background was also adopted to calculate the cooling due to primordial species.

Metal cooling depends on redshift because the radiation background evolves with time. Although our simulations traced the formation of alpha elements and iron separately, our metal cooling assumed relative solar abundances for simplicity. We used the CLOUDY default solar composition, which contains the first thirty elements in the periodic table (Data compiled from Grevesse & Sauval (1998); Holweger (2001); Allende Prieto et al. (2001, 2002), see Ta-

ble 9 of the CLOUDY version 07.02 documentation for details). The metal cooling rates were calculated by subtracting the primordial cooling rates from the cooling rates of the total 30 elements, including H and He. We found that the net metal cooling rate is linear with metallicity, which allows us to tabulate the rates for solar abundance only and scale with metallicity (equation 5). The metal cooling rates can thus be written as:

$$\Lambda_{\text{metal}}(T, \rho, z, Z) = \frac{Z}{Z_{\odot}} \Lambda_{\text{metal}, \odot}(T, \rho, z) \quad (5)$$

where  $T$ ,  $\rho$ ,  $z$  and  $Z$  are the temperature, density, redshift and metallicity of the gas, respectively.

The metal cooling rates were tabulated in  $\log(T)$  (in unit of K, from 100 K to  $10^9$  K with  $\Delta \log(T) = 0.05$ ),  $\log(n_H)$  (where  $n_H$  is the hydrogen number density, from  $10^{-9} \text{ cm}^{-3}$  to  $10^3 \text{ cm}^{-3}$  with  $\Delta \log(n_H) = 0.1$ ), and redshift  $z$  ( $8.9 \leq z \leq 0$  with grid size 0.1). The cooling and heating rates were interpolated separately in log space in the simulation. The RMS of relative interpolation errors for cooling and heating are less than 1 percent. We assumed the gas was optically thin to the ionizing background for all wavelengths, which is valid for the IGM. We included metal cooling down to 100 K which can occur in dense environments or in the IGM that is cooled by adiabatic expansion, although the latter is generally not not enriched. At low temperature we turned off the molecular hydrogen cooling, because  $H_2$  in the IGM is not in ionization equilibrium and CLOUDY gave unrealistically high  $H_2$  cooling rates by assuming equilibrium (also see Smith et al. (2008)). Beyond  $z > 8.9$  cooling was calculated with effectively no UV background.

Figure 1 shows cooling rates normalized by  $n_H^2$  as a function of temperature at various metallicities. The black curves show the total cooling rates with  $z=3$  radiation background, while the red curves show the CIE metal cooling (no UV) plus the cooling of H and He under the UV background, a model often adopted in cosmological simulations. With or without UV, the presence of metals can increase cooling rates by up to several orders of magnitude. In the temperature range  $10^4 < T < 10^8$  K, radiation ionizes the plasma and reduces the number of ions that can be collisionally excited therefore decreases the cooling rates significantly (e.g., about an order of magnitude at  $10^5$  K in Figure 1). The cooling peak also shifts from  $10^5$  K to  $10^6$  K due to the change of ionization states of the metal elements. From 100 K to  $10^4$  K, the UV background increases the number density of free electrons ( $n_e$ ) hence enhancing forbidden line cooling from low ionized species such as C I, C II, Si I, Si II and O I. Forbidden line cooling is the dominant cooling process in enriched IGM at low temperatures. At low densities ( $n_H \lesssim 10^{-4} \text{ cm}^{-3}$ ), photo-ionization also creates some higher-ionized species with strong magnetic dipole transitions (e.g. Ne V and Ne VI). These ions can cool the plasma more efficiently, producing a local cooling peak around  $10^3$  K (Figure 1). However with an increase in density these ions disappear and the major coolants are the less ionized species mentioned, consistent with ISM cooling models (e.g. Wolfire et al. 2003). Overall, the radiation background increases the metal cooling rate substantially between 100 K and  $10^4$  K over CIE. Figure 1 shows unequivocally that simply adding the CIE model of metal cooling on the primordial cooling rates results in dramatic over or under estimation of

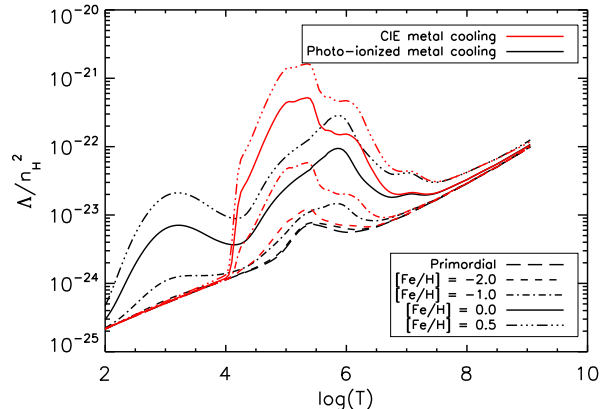


**Figure 1.** Cooling rates normalized by  $n_H^2$  (in  $\text{erg s}^{-1} \text{ cm}^3$ ) with metallicities  $[\text{Fe}/\text{H}] = -2.0, -1.0, 0$  and  $0.5$ . The gas has density  $n_H = 10^{-5} \text{ cm}^{-3}$ . *Black*: total cooling rates (include H, He and metals) under the  $z=3$  extragalactic radiation background from Haardt & Madau (2005); *Red*: Sum of cooling rates of H and He under the same radiation background, and metal cooling rates, calculated without UV background

the cooling rates, depending on the temperature. The amplitude of the UV background used here is however too high, as implied in the Lyman  $\alpha$  flux decrement evolution in Section 3.3. Thus the effect of photo-ionization on metal cooling rate may be overestimated.

## 2.2 Turbulent Metal Diffusion

As a Lagrangian particle method, SPH does not include any implicit diffusion of scalar quantities such as metals. Wadsley, Veeravalli & Couchman (2008) demonstrated that this has physically incorrect consequences for even simple processes such as convection and Rayleigh-Taylor instabilities. Including a simple model for turbulent mixing (using a diffusion coefficient,  $D = C \Delta v h_{\text{SPH}}$  based on the pairwise velocity,  $\Delta v$ , at the resolution scale,  $h_{\text{SPH}}$  and  $C \sim 0.1$ ) Wadsley, Veeravalli & Couchman (2008) were able to match Eulerian grid code results (which must mix due to the necessary advection estimates). In particular, it became possible to generate similar non-radiative galaxy cluster entropy profiles with SPH as with high resolution grid codes. This was a major discrepancy in the Frenk et al. (1999) cluster comparison. Greif et al. (2009) implemented a similar scheme and applied it to simulating supernova remnants. As discussed previously, galactic outflows should be highly turbulent and thus mixing is essential for IGM studies.

Turbulent mixing models have a long history in environmental and engineering fluid mechanics. GASOLINE now incorporates a more robust mixing estimator similar to that first proposed by Smagorinsky (1963) for the atmospheric boundary layer,

$$\begin{aligned} \frac{dA}{dt} \Big|_{\text{Diff}} &= \nabla \cdot (D \nabla A), \\ D &= C |S_{ij}| h^2, \end{aligned} \quad (6)$$

where  $A$  is any scalar, we use the trace-free shear tensor for  $S_{ij}$  and  $h$  is the measurement scale (here  $\sim h_{\text{SPH}}$ ). This

choice for  $S_{ij}$  results in no diffusion for compressive or purely rotating flows. In SPH terms the diffusion expression for a scalar  $A_p$  on particle  $p$  is computed as follows,

$$\begin{aligned}\tilde{S}_{ij|p} &= \frac{1}{\rho_p} \sum_q m_q (v_{j|q} - v_{j|p}) \nabla_{p,i} W_{pq}, \\ S_{ij|p} &= \frac{1}{2} (\tilde{S}_{ij|p} + \tilde{S}_{ji|p}) - \delta_{ij} \frac{1}{3} \text{Trace } \tilde{S}|_p, \\ D_p &= C |S_{ij|p}| h_p^2, \\ \frac{dA_p}{dt}|_{\text{Diff}} &= - \sum_q m_q \frac{(D_p + D_q)(A_p - A_q)(\mathbf{r}_{pq} \cdot \nabla_p W_{pq})}{\frac{1}{2}(\rho_p + \rho_q) \mathbf{r}_{pq}^2},\end{aligned}\quad (7)$$

where the sums are over SPH neighbours,  $q$ ,  $\delta_{ij}$  is the Kronecker delta,  $W$  is the SPH kernel function,  $\rho_q$  is the density,  $\mathbf{r}_{pq}$  is the vector separation between particles  $v_{i|q}$  is the particle velocity component in direction  $i$ ,  $\nabla_p$  is the gradient operator for particle  $p$  (operating on the SPH kernel function) and  $\nabla_{p,i}$  is the  $i$ th component of the resultant vector. The difference between this model and the ones used in Wadsley, Veeravalli & Couchman (2008) and Greif et al. (2009) is that the diffusion coefficient is calculated according to a turbulent mixing model instead of simply using velocity differences. The coefficient depends on the velocity shear hence it better models the mixing in shearing flows. On the other hand, if there is no shearing motion between two phases of fluids (such as a clumpy medium embedded in hot wind fluid and the two move with same speed), then no turbulent diffusion is added. The Smagorinsky model has also been used successfully in other field such as weather modeling.

A coefficient value of order 0.05 – 0.1 is expected from turbulence theory (depending on the effective measurement scale,  $h$ ). It was found that a conservative choice of  $C = 0.05$  was sufficient to match the cluster comparison. This diffusion was applied to thermal energy and metals in all runs except “nmd\_40\_256”. Diffusion of density results naturally from the noise in the velocity field which moves particles around.

### 3 GLOBAL PROPERTIES OF THE SIMULATION

Before embarking on a detailed examination of the metal distribution and evolution in the IGM, it is worth establishing the basic properties of the simulated volume with respect to the star formation history (SFH), the Lyman- $\alpha$  forest and the evolution of total neutral hydrogen. These properties directly reflect the effectiveness of the feedback processes and allow the approach to be calibrated with respect to observations.

#### 3.1 Star Formation History

Figure 2 shows the evolution of global star formation rate (SFR) as a function of redshift. The observational data with error bars were adapted from Hopkins (2004) and scaled to the same IMF and cosmology as used in our simulations. The figure shows that all simulations with moderate resolution (with or without metal cooling and diffusion) produce the SFH that is consistent with observations for  $z \gtrsim 0.5$ .

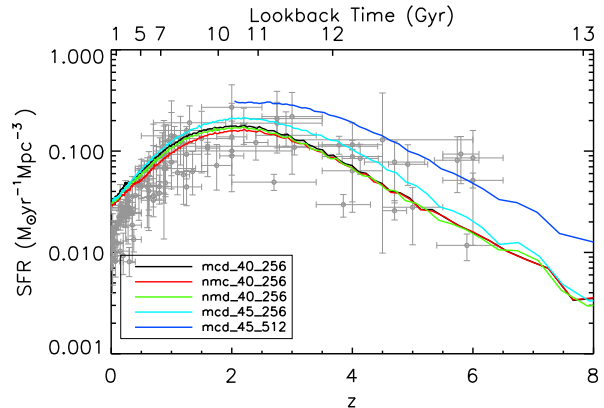


**Figure 2.** Star formation rate (SFR) density (in unit of  $M_{\odot} \text{ yr}^{-1} \text{ Mpc}^{-3}$ ) as a function of redshift. Data were compiled from Hopkins (2004) and scaled to the same IMF and cosmology as in our simulations. The moderate resolution simulations give SFR consistent with observations down to redshift 0.5. The high resolution run has significantly higher SFR but still in broad agreement with observations.

The peak of star formation lies around  $z \sim 2$  for all simulations. Without superwind models, Springel & Hernquist (2003) and Oppenheimer & Davé (2006) found higher SFR than the observations and the SFH is peaked at  $z \sim 4$ . Our results suggest that the suppression of SFR can also be attained using feedback models without explicit winds. Until  $z \sim 0.5$ , our  $256^3$  simulations show no overproduction of stars while matching other observables. Note that while the  $512^3$  does show high SFR, it was a direct convergence test with all parameters fixed. The parameters affecting SF efficiency should be adjusted downwards with increasing resolution for consistent outcomes at  $z = 0$  (c.f. Stinson et al. 2006).

The simulations do form too many stars at  $z < 0.5$ . One possible reason is that AGN feedback becomes more relevant at lower redshift, and the supermassive black holes in these objects can generate strong AGN feedback effects. Since AGN were not included in our model, the global SFR is higher than observations.

The simulation without metal cooling produced fewer stars at  $z < 5$ . The difference in SFR between the simulations with and without metal cooling increases from  $\sim 5\%$  at  $z = 4$  to  $\sim 20\%$  at  $z = 1$ , then decreases to  $10\%$  at  $z = 0$ . Metal cooling enhances the cooling of the IGM and therefore its accretion rate onto galaxies. Choi & Nagamine (2009) also found enhancement of SFR with metal cooling, though their SFR was generally enhanced by 20% to 30% over all redshifts below  $z = 15$ , and in some runs by 50% at  $z = 1$ . The discrepancy may result from their adoption of Sutherland & Dopita (1993) metal cooling rates that are significantly higher than what we used, since it does not include the radiation background. However, Schaye et al. (2010) used the cooling model from Wiersma et al. (2009a) which also includes the suppression of metal cooling by UV background, yet still found a larger enhancement of SFR comparable to Choi & Nagamine (2009). This is possibly due to the higher metallicities in stars and the ISM in their

simulations (Wiersma et al. 2009b). In particular, they included mass loss by AGB stars which may largely contribute to the enrichment of the ISM.

The simulation without metal diffusion (but with metal cooling) also produced slightly fewer stars (about 6 % mean) than the reference run at  $z < 4$ , because metal diffusion allows enriched particles to mix their metals, so more particles experience metal cooling and turn into stars. On the other hand, the metallicities of the original enriched particles are reduced because of the diffusion, thus those particles have less strong cooling hence are less likely to form stars. Our result suggests that the first factor dominates. Since the effect of metal diffusion relies heavily on metal cooling, it is smaller than in the case where the metal cooling was turned off.

The effect of resolution on the SFH is shown in the convergence runs “mcd\_45\_256” (cyan) and “mcd\_45\_512” (blue). At  $z = 8$ , the high resolution run produces 3 times larger SFR. Although the result does not converge by  $z = 2$ , the difference between these two runs does steadily decrease with time. At  $z = 2$ , it reaches about 50%. The SFH from “mcd\_45\_512” is close to the high end of the observational data but still consistent with them. The increased star formation is the same magnitude seen in the convergence tests in Stinson et al. (2006), where it was determined that higher resolution simulations produce more high density gas. High density gas forms more stars either because it surpasses the density threshold where gas in the low resolution simulations does not, or because star formation is a function of gas density in the Kennicutt-Schmidt law. Since the difference is most prominent in the early epochs of our simulations when galaxies are small, it is likely that many dwarf galaxies surpass the gas density threshold in the high resolution that do not in the low resolution simulations. The effect of initial condition variation is also worth noting: the “mcd\_45\_256” run has slightly lower (but comparable) resolution than the reference run. However, it has a higher SFR at  $z > 1$ .

### 3.2 Evolution of $\Omega_{\text{HI}}$

The evolution of the cosmic mass density in neutral hydrogen ( $\Omega_{\text{HI}}$ ) with redshift and its relation to stellar mass density is one of the key observables for understanding the interaction between gas and galaxies. Observations of damped Ly- $\alpha$  systems (DLAs) (Prochaska et al. 2005; Rao et al. 2006; Prochaska & Wolfe 2009) and the H I 21-cm emissions (Zwaan et al. 2005; Lah et al. 2007) (shown in Figure 3) suggest that  $\Omega_{\text{HI}}$  does not evolve substantially through cosmic time, even though the stellar mass density keeps increasing. This implies that there is a steady supply of gas cooling onto galaxies, providing fuel for star formation. The decrease of H I at  $z \sim 2.3$  has been linked to violent feedback processes, including SN, galactic winds and AGN activities (Wolfe et al. 2005; Prochaska & Wolfe 2009), but it is not clear why the amount of H I increases back at  $z < 2.3$ . Prochaska & Wolfe (2009) argued that the data at  $z \lesssim 2$  was biased high and  $\Omega_{\text{HI}}$  should remain constant from  $z = 2.2$  to  $z=0$  (the last 10 Gyrs). The non-evolution of  $\Omega_{\text{HI}}$  indicates that star formation is self-regulated such that gas accretion, star formation and feedback processes balance each other. Numerical simulations without mass loss through winds (Cen et al. 2003) found  $\Omega_{\text{HI}}$  is several

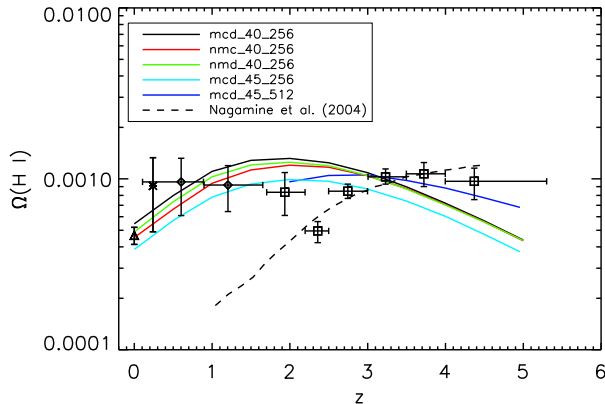
times higher. Nagamine et al. (2004a) included the superwind model from Springel & Hernquist (2003) in their simulations so that neutral gas could be ejected from the galaxies, which produced the correct amount of  $\Omega_{\text{HI}}$  at  $z > 2$ , but at  $z < 2$  too much material was blown away, resulting in a deficit of  $\Omega_{\text{HI}}$  (dash line in Figure 3).

Figure 3 shows the evolution of  $\Omega_{\text{HI}}$  in our simulations. Because most neutral hydrogen resides in damped Ly- $\alpha$  systems, which are clouds with H I column densities larger than  $2 \times 10^{20} \text{ cm}^{-2}$  (Wolfe et al. 2005, and references therein), the gas is mostly self-shielded from external ionizing photons. Self-shielding was not modeled during the simulations, however we used a radiative transfer post-processor to recalculate the ionization states of hydrogen as described in Pontzen et al. (2008). The ionizing background was the standard Haardt & Madau (2005) reduced by a factor of 2 (as discussed in section 3.3 below). However, variations of this magnitude have practically no impact on the dense gas that dominates  $\Omega_{\text{HI}}$ .

Figure 3 shows that after we applied the self-shielding correction, our feedback model produced similar  $\Omega_{\text{HI}}$  to observations from  $z \sim 3.5$  down to  $z = 0$  for the runs with moderate resolutions. At higher redshift these simulations underestimate  $\Omega_{\text{HI}}$ , possibly because of insufficient resolution (discussed below). The result indicates that our feedback models effectively moderate star formation but not too strongly, so that gas accretion onto disks is not disrupted. Thus it can maintain the steady supply of neutral hydrogen to galactic disks. The shape of the  $\Omega_{\text{HI}}$  relation follows the SFH, which reflects the relation between the H I density and SFR density, i.e. the Schmidt Law for star formation. The decrement at  $z = 2.3$  is not reproduced in our simulations, indicating that more violent feedback maybe necessary at this limited redshift range if this feature is confirmed. We will investigate wind models in high resolution single galaxy and galaxy groups in future work.

As expected, Figure 3 shows that metal cooling and metal diffusion increases the amount of neutral hydrogen. The metal cooling effect is obvious at  $z \lesssim 3$  and at  $z = 0$  the increase is  $\sim 17\%$ . Metal diffusion has a smaller effect. The reasons for these effects are similar to the ones discussed in SFR analysis in section 3.1.

With eight times higher resolution, the simulation “mcd\_45\_512” produces a significantly higher  $\Omega_{\text{HI}}$  and a flatter curve at  $z > 2.5$  which make the result compare better with observations. At  $z = 5$ , the high resolution run contains about 80% more neutral hydrogen. At  $z = 2$  the  $\Omega_{\text{HI}}$  curve joins the moderate resolution run “mcd\_45\_256” but has a slightly steeper decreasing slope towards lower  $z$ . The difference in  $\Omega_{\text{HI}}$  is likely because the high resolution run better resolves small halos, thus increasing the amount of self-shielded gas. Since small halos dominate at high redshift, the difference is most obvious there. We note that as a result of cosmic variance the “mcd\_45\_256” simulation contains 15-30% less HI throughout the simulation than the fiducial run even though it has a higher SFR. Thus the relationship between SFR and the gas reservoir  $\Omega_{\text{HI}}$  is not always monotonic as seen in the cases for “nmc\_40\_256” and “nmd\_40\_256”. Higher SFR consumes more neutral gas thus may decrease the amount of  $\Omega_{\text{HI}}$ .



**Figure 3.** Evolution of total neutral hydrogen density in units of critical density today ( $\Omega_{\text{HI}}$ ). Observational data points: *Square*: Prochaska et al. (2005); *Diamond*: Rao et al. (2006); *Asterisk*: (Lah et al. 2007); *Triangle*: Zwaan et al. (2005).

### 3.3 Lyman- $\alpha$ Flux Decrement

The Lyman- $\alpha$  forest traces the neutral hydrogen in the diffuse IGM. Since the IGM is optically thin, the mean flux decrement of the Lyman- $\alpha$  forest,  $D_{\text{Ly}\alpha}$ , is sensitive to the UV radiation and can be used to calibrate the UV background in simulations. We generated the *Ly* -  $\alpha$  spectra by tracing a lines of sight through every simulation box. Each line of sight consists 25 lines segments, which were spread through the entire box such that the periodicity of the box was used to eliminate any discontinuity in the resulting spectra. Particles that lay within two smoothing lengths measured perpendicularly to their closest line segments contributed to the absorption along the line, and the amount of contribution was weighted using the SPH smoothing kernel. The particles’ peculiar velocity, thermal velocity and Hubble expansion were all taken into account. The H I, He I and He II fractions were calculated during the simulation as described in Section 2.1. The Ly- $\alpha$  optical depth at each velocity due to Doppler broadening was calculated and then convolved with the Lorentz profile.

Figure 4 depicts the evolution of  $D_{\text{Ly}\alpha}$  compared to the observations of Bernardi et al. (2003), Schaye et al. (2003), Kirkman et al. (2007) and Faucher-Giguère et al. (2008). When we attenuate the UV spectrum by factor of 2, our results agree with most observations up to  $z \sim 3.5$ . At higher redshift, our results are slightly lower than, but still broadly consistent with the observational data. The biggest difference is seen when comparing to Bernardi et al. (2003). The discrepancy may indicate that more UV attenuation for  $z \gtrsim 3$  in our simulation is necessary. However, observations of the Ly $\alpha$  forest at high redshift may be subject to large uncertainties due to the continuum correction (Bernardi et al. 2003) and metal line contamination (Schaye et al. 2003). The Schaye et al. (2003) and Faucher-Giguère et al. (2008) data are contamination corrected and our result compare better with these data. Hence, a factor of 2 seems sufficient and we use this value for all subsequent calculations. This attenuated UV background is only used in the analysis, but not in the entire simulation. Although for the diffuse, highly ionized primordial IGM, the effect of photo-ionization on gas

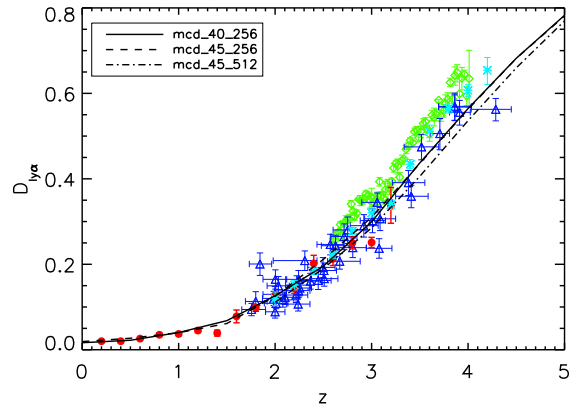


**Figure 4.** The evolution of the mean flux decrement of the Ly- $\alpha$  forest from our reference simulation (“mcd\_40\_256”) and the convergence test (“mcd\_45\_256” and “mcd\_45\_512”). Color symbols with error bars indicate the observational data. *Green diamond*: Bernardi et al. (2003), data here are derived from their original evolution of effective optical depth,  $\tau_{\text{eff}}$  in their Fig. 4; *Blue triangle*: Schaye et al. (2003), data here are derived from the original  $\tau_{\text{eff}}$  after removal of pixels contaminated by metal lines (Table 5); *Red solid dot*: Kirkman et al. (2007); *Cyan asterisk*: Faucher-Giguère et al. (2008), derived from their  $\tau_{\text{eff}}$  evolution after contamination correction (Table 1).

dynamics is small (Croft et al. 1998), UV does affect metal cooling and hence star formation. Thus, by using the original UV background without attenuation, our metal cooling calculation may have overestimated the effect of photo-ionization. However, along with other workers, we are also neglecting local ionizing sources which correct the UV upward to a significantly greater extent within galaxies. These details of ISM physics are potentially important but beyond current capabilities where we must rely upon relatively crude ISM models.

Focusing on the convergence test, with high resolution (dot-dashed line) the Ly $\alpha$  decrement evolves very similarly with redshift, but is a few percent smaller than the lower resolution (dashed line) run. The decrease in  $D_{\text{Ly}\alpha}$  is consistent with the increase in SFR and  $\Omega_{\text{HI}}$ . It can be interpreted as when more gas accretes onto galaxies and forms stars for high resolution, the H I content in the IGM (probed by the Ly $\alpha$  forest) decreases.

## 4 EVOLUTION OF GAS, METAL FRACTIONS AND METALLICITY

We now examine the enrichment of the IGM through the metal distribution in different gas phases. We examine how they evolve and the effect of the metal diffusion and cooling. The gas phases were defined using the convention of Wiersma et al. (2009b). All the gas that has hydrogen number densities  $n_{\text{H}} > 0.1 \text{ cm}^{-3}$  is star forming gas (SF gas). Of all the non-star forming gas (non-SF gas), gas with  $10^5 \text{ K} < T < 10^7 \text{ K}$  is the warm-hot intergalactic medium (WHIM) and gas with  $T > 10^7 \text{ K}$  is the intracluster medium (ICM). Of the cooler medium ( $T < 10^5 \text{ K}$ ), that with overdensity  $\rho/\rho_{\text{mean}} > 100$  is associated with galactic halos,

while that with  $\rho/\rho_{mean} < 100$  is the diffuse IGM. Note that these definitions are somewhat arbitrary and there is no well-defined border for each gas phase. In particular, at low redshift substantial part of the WHIM comes from the shock-heated gas accreting onto galaxies so it is likely to be associated with galactic halos. However, by this definition gas is roughly divided according to its location and key physical processes.

#### 4.1 Evolution of Gas and Metal Fractions

Figure 5 shows how the gas and metal fractions evolve. The left panels focus on the mass fractions in gas and stars. Almost all baryonic mass is in the diffuse IGM at  $z=7$ . By  $z=0$ , the mass fractions in stars, the diffuse IGM and the shock heated WHIM are about 20%, 40% and 40%, respectively for the moderate resolution runs. The stellar mass fraction at  $z=0$  is consistent with observations (Wilkins et al. 2008, and references therein), although close to the high end. A large amount of WHIM forms at low redshift when gas is shock heated when falling into halos. The mass fraction of WHIM gas is consistent with SPH simulations using explicit galactic superwind models (Oppenheimer & Davé 2006; Choi & Nagamine 2009), and Eulerian simulations (Cen & Ostriker 2006). The amount of star forming gas (ISM) and galactic halo gas evolves similarly to the SFH shown in Figure 2, reflecting a close relation between the ISM, halo gas and SF activity.

The blue and cyan lines in Figure 5 show the convergence of mass fractions. At high redshift, the  $512^3$  simulation has a larger mass fraction in stars, the ISM, halo gas and the WHIM. Resolving smaller halos at large  $z$  increases the amount of gas in galaxies (halos and the ISM) and enhances SF. Consequently, enhanced stellar feedback increases the amount of WHIM. This effect is more significant at higher redshift and decreases with time. The WHIM fraction converges at  $z < 4$ . The ISM and halo gas fractions reach similar values as in the low resolution run at  $z=2$ , although they seem to decline slightly faster towards low  $z$ . For the stellar mass, however, there is about 37% more in the high resolution run at  $z=2$ . Although it is still difficult to predict the stellar fraction at  $z=0$ , we expect that the difference will be lower at  $z=0$  since there is already no excess in the reservoir gas (the ISM) at  $z=2$ . In fact, early star formation seen in the high resolution simulation may consume the gas that would otherwise contribute to SF at low redshift, hence the SFR may decline faster towards low  $z$ , which may imply a rapid convergence in stellar mass fraction.

The right panels of Figure 5 show how the metal fractions present in stars and different gas phases evolve. At  $z=7$ , gas (SF and Non-SF) contains the majority of the metals while stars contain only a few percent, which is possibly because the time scale for gas consumption is longer than the age of the Universe, so that metals in the ISM do not have enough time to be incorporated into stars. With metal diffusion, initially the non-SF gas (the IGM + halo gas) and the SF gas (i.e. the ISM) contain comparable amounts of metals, with the former having slightly more in most runs. With time, the metal fraction in the non-SF gas decreases and the metals budget is dominated by the ISM and later by stars. As  $z=0$ , 80% to 90% of metals reside in stars. The IGM and halo has about 10% of the metals and the ISM

has only a few percent. The result that the IGM contains a larger fraction of metals at higher redshifts suggests that the enrichment process is very efficient at early epochs, possibly because it is easier for wind material to leave the shallow potential wells of early objects. For different phases of the IGM, metal fractions in both the WHIM and the diffuse IGM decrease with time. For example, in the standard run, the WHIM metal fraction decreases from  $\sim 40\%$  at  $z=7$  to about 10% at  $z=0$ , the metal fraction in diffuse IGM decreases from  $\sim 10\%$  to  $\sim 1\%$ . The ICM, on the other hand, increases its share of metals as galaxy clusters form at low redshift.

Metals in the IGM are primarily in the WHIM, with a smaller fraction in the diffuse IGM. This remains the case for the entire cosmic history, which differs from Davé & Oppenheimer (2007), who found that most metals reside in the cooler diffuse IGM from  $1.5 < z < 6$ . This is probably because they use hydrodynamically decoupled, kinetic feedback. Their superwinds were generated in cold SF gas and hydrodynamically decoupled when they left the ISM, and the wind material was likely to be cool. Our feedback model ejects SN energy into the surroundings and suppresses the gas cooling and the winds are generated by thermal pressure, which makes them more likely to be hot and in the WHIM phase. Wiersma et al. (2009b) obtained a similar result as ours for the IGM metals using a local energy injection and hydrodynamically coupled wind model from Dalla Vecchia & Schaye (2008). However, metals in their simulations mostly reside in the ISM at redshift  $z > 2$  while in our results the IGM generally contains more metals at high redshift. While more controlled simulations are necessary to explain the difference, it seems that subgrid feedback models alter metal enrichment significantly.

The high resolution simulation increases the metal fraction in stars while decreasing it in the ISM and Non-SF gas. Between different phases of the Non-SF gas, halo gas and the diffuse IGM increase their shares of metals, while metal fractions in the WHIM decreases. This is expected since with high resolution SN feedback events are more frequent but each has smaller impact. As a result, particles that receive feedback energy and metals generally have shorter cooling shut-off times in the blastwave model (Stinson et al. 2006). Thus they can be cooled more efficiently by metal cooling to the diffuse IGM, or to the cool halo gas. No clear convergence is seen at  $z=2$  when the high resolution simulation was terminated. The differences in stars, the ISM, halo gas and the WHIM are 17%, 25%, 14% and 41%, respectively. However the trend of metal fraction evolution as a function of redshift remains similar for high and low resolution runs. The general conclusions about enrichment efficiency and about metal distribution in each phases also remain the same.

#### 4.2 Evolution of Metallicity

Figure 6 shows how the mass weighted metallicity in stars and the gas phases evolves. Stars and SF gas have the highest metallicities throughout the simulation. The metallicities are about  $10^{-2} Z_{\odot}$  at  $z=6-7$  and steadily increase to  $\sim 0.5$  solar at  $z=0$ . At  $z=0$ , the value is in agreement with the observed stellar metallicities in galaxy groups,  $Z_{\star} \sim 0.6 Z_{\odot}$  (Finoguenov et al. 2003) and simulation results from

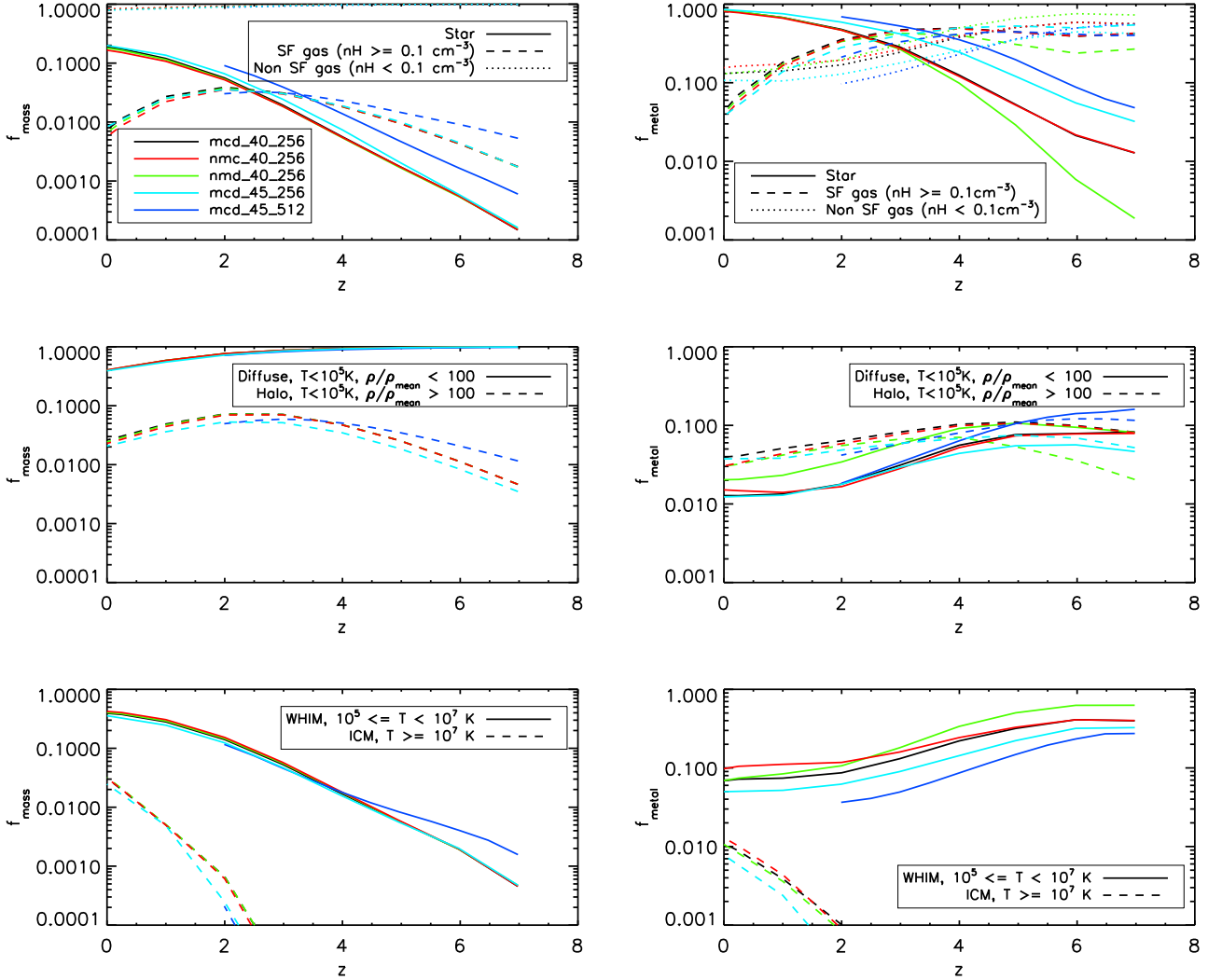


**Figure 5.** The evolution of baryon mass and metal fraction in various gas phases and stars. The gas is divided as star forming gas, diffuse IGM, halo gas and WHIM according to the definition described in the text. *Black*: the standard run “mcd\_40\_256”. *Red*: the run with metal cooling turned off. *Green*: the run with no metal diffusion. *Cyan*: medium resolution run in the convergence test “mcd\_45\_256”. *Blue*: high resolution run “mcd\_45\_512”. The meaning of each line type in each panel is defined by the legends in that panel.

Davé & Oppenheimer (2007). However, it is about 0.5 dex lower than the measurement from Gallazzi et al. (2008) (diamond symbol in left upper panel of Figure 6), although our total stellar metal density ( $\Omega_Z$ ) is  $4\text{--}5 \times 10^{-5}$  at  $z = 0$ , consistent with the Gallazzi et al. (2008) value. At  $z = 2$ , the stellar metallicity is consistent, but slightly lower than the observation by Halliday et al. (2008).

Metallicities of stars and SF gas are similar throughout the simulation. The non-SF gas has an overall similar trend of evolution as the stars and SF gas, but is less enriched on average. The metallicity of the diffuse IGM evolves significantly but is much less enriched comparing to other phases. At  $z=0$  it is only  $10^{-2.5} Z_\odot$ . The metallicities of the WHIM and the ICM evolve slowly with a slight decreasing trend, despite their rapid mass increase at low redshift. Both values vary between  $0.01 Z_\odot$  and  $0.1 Z_\odot$ . Since WHIM and the cool diffuse IGM contains similar mass at  $z = 0$ , the fact that WHIM metallicity is much higher than the diffuse gas

implies our IGM enrichment process happens primarily in the WHIM. The convergence is better for metallicity than metal fractions, and the metallicities of most gas phases are nearly converged at  $z = 2$ . The largest difference is seen for diffuse IGM and the halo gas, where the high resolution run has about 43% and 26% higher metallicities, respectively. It may be because feedback gas has a shorter cooling shut-off time so it is more likely to cool to  $< 10^5$  K, or because the high resolution run can better resolve star formation in smaller halos at higher redshift, and the metals ejected from those objects have not been heated above  $10^5$  K.

We computed the mean metallicities of the halo gas and the ISM and compared it with the metallicity evolution of the DLAs and sub-DLAs from Prochaska et al. (2003) (triangle symbols in the bottom right panel of Figure 6). The DLA and sub-DLA systems are considered tracing the gas in galactic disks and halos. Our results compare well with observations in this case. We also compare the diffuse

IGM metallicity with observations using C IV (Schaye et al. (2003), square symbol) and O VI (Aguirre et al. (2008), cross symbol) at  $z \sim 2.5$ . Our results are smaller than both observations even for the high resolution case. Since the results do not converge here, this discrepancy could be due to a lack of resolution. Alternatively, it may also suggest additional feedback mechanisms which can enrich diffuse IGM are probably necessary here. For the intracluster medium, observations found higher metallicities than our results at  $z=0$ , about  $0.2 - 0.5 Z_{\odot}$  (Aguirre & Schaye 2007, and references therein). This inconsistency may be because of the AGN feedback absent in the simulations. Moreover, the size of our simulation also limits the number of galactic clusters that can form (below the cosmic average). Since our simulations were designed for studying metal enrichment in the IGM, we will not further address the intracluster medium.

### 4.3 The Effects of Metal Cooling and Metal Diffusion

#### 4.3.1 The Effects of Metal Cooling

The red curves in the left panels of Figure 5 show the evolution of mass fraction without metal cooling. At  $z = 0$ , metal cooling increases the stellar and halo mass fraction each by  $\sim 14\%$ , increases the SF gas fraction by  $32\%$ , and decreases the WHIM fraction by  $7\%$ . It reflects that metals enhance the cooling significantly at WHIM temperatures ( $10^5 K - 10^7 K$ ) and thus more WHIM cools onto galaxies and forms stars. The mass of diffuse IGM is almost unaffected by metal cooling ( $\sim 1\%$  decrease at  $z = 0$ ) as its metallicity is very low, as shown in Figure 6.

The right panels of Figure 5 show that the metal cooling decreases the metal fraction in the WHIM and increases it in the halo gas and the SF gas, because it enhances the cooling of enriched WHIM onto galactic halos and disks. At  $z=0$ , the decrease in WHIM gas is  $\sim 24\%$ , the increase in halo gas is  $\sim 42\%$ . For stars and SF gas the increments are  $14\%$  and  $32\%$ , respectively. For the WHIM and the halo gas, the effects of cooling in metal fractions (which traces the enriched gas) are larger than in mass fractions (which traces the total gas). For star and SF gas, the effect of metal cooling is similar in both mass and metal fractions. For the diffuse IGM, metal cooling increases its metal fraction at  $z > 1.5$ , but decreases it at lower redshift. The early increase is likely due to the cooling of WHIM to become diffuse IGM, while the later decrease is probably because of the diffuse IGM itself is enriched enough so that metal cooling can enhance its accretion onto halos.

#### 4.3.2 The Effects of Metal Diffusion

Metal diffusion produces similar effects as metal cooling on mass fraction. Metal diffusion contaminates large amounts of otherwise pristine gas with metals, enabling it to cool through metal lines from WHIM to SF gas or halo gas, and enhances the SFR. As it depends on the metal cooling, the effects of metal diffusion on mass fraction are smaller in magnitude than having metal cooling off (similar to the effects on the SFH). At  $z = 0$ , the increase in halo and stellar mass fractions are about  $7\%$  and  $5\%$ , respectively, and the decrease in WHIM is  $\sim 3\%$ .

The green curves in the right panels of Figure 5 show the direct impact of metal diffusion on the metal content of various gas phases. Metal diffusion increases the metal content of stars, the ISM and halo gas (i.e., gas in the galaxies), and decreases the metal content of the WHIM, the ICM and the diffuse IGM (i.e., the IGM). This is counter intuitive since one expects diffusion to distribute the metals more evenly. However, as the enriched gas is ejected out of the galaxies, metal diffusion mixes its metals with the ambient gas (i.e., the ISM and the galactic halos) along the outflow trajectory so that by the time the outflow reaches the IGM (WHIM, diffuse gas or the ICM), its metal content has decreased. In other words, diffusion prevent highly enriched gas from transporting all its metals to the WHIM. This is further discussed in Section 5. Metal diffusion may alleviate the problem found in previous SPH simulations where the metals are too inhomogeneous (e.g., Aguirre et al. 2005). We will make a detailed analysis of the effects of metal diffusion in observable ions such as C III, C IV and O VI in a future paper.

The impact of metal diffusion changes with redshift. It is more significant at high redshift for the WHIM, the halo, the ISM and the stars. For example, from  $z = 7$  to  $z = 0$ , the increase in star metal fraction varies from  $0.4\%$  to  $580\%$ , in SF gas from  $7\%$  to  $\sim 60\%$ , in halo gas from  $30\%$  to  $300\%$ . The decrease in the WHIM metal fraction varies from  $0.6\%$  to  $60\%$ . Since diffusion arises from velocity shear, the diffusion effects are high near winds. The concurrent decrease in the WHIM metals and the increase in stellar, SF or halo metals imply that the winds take metals from galaxies directly to the WHIM. The fact that the diffusion impact is higher at high redshift suggests that the winds between these phases are more effective at early times.

## 5 DISTRIBUTION OF GAS AND METALS IN DENSITY AND TEMPERATURE AT $Z=0$

In this section, we examine the detailed distribution of mass and metals in the density-temperature ( $\rho$ - $T$ ) phase diagram at  $z=0$ . In Figure 7, the green contours indicate the mass distribution of gas across the phase diagram while the labeled darker contours indicate mean metallicities for that gas. The left panel shows the standard run while the right panel has diffusion turned off. Looking at the standard run, it can be seen that gas with  $T < 10^4 K$  and  $\rho < 10 \rho_{mean}$  follow a power law equation of state (EOS). It is heated by photoionization and cooled by adiabatic expansion and has generally not participated in star formation or feedback, following the standard expectation for the diffuse IGM (e.g. Hui & Gnedin 1997). At  $\rho > 10 \rho_{mean}$ , the gas distribution splits into high and low temperature branches. The low temperature branch extends to star-forming gas in galaxies. Due to metal cooling, gas with  $\rho > 10^4 \rho_{mean}$  can reach temperatures below the atomic hydrogen cooling cut-off at  $\sim 10^4 K$ . The WHIM is apparent as the less dense gas with temperatures above  $10^5 K$ . There is less gas around  $\sim 10^{5.5} K$  compared to the peaks at  $10^4 K$  and  $10^{6.5} K$  due to the peak in metal cooling rates at  $10^5$  to  $10^6 K$ .

The WHIM arises from both metal enriched winds and pristine virial shocks. Wind material can get out to very low densities but with realistic diffusion operating the typical

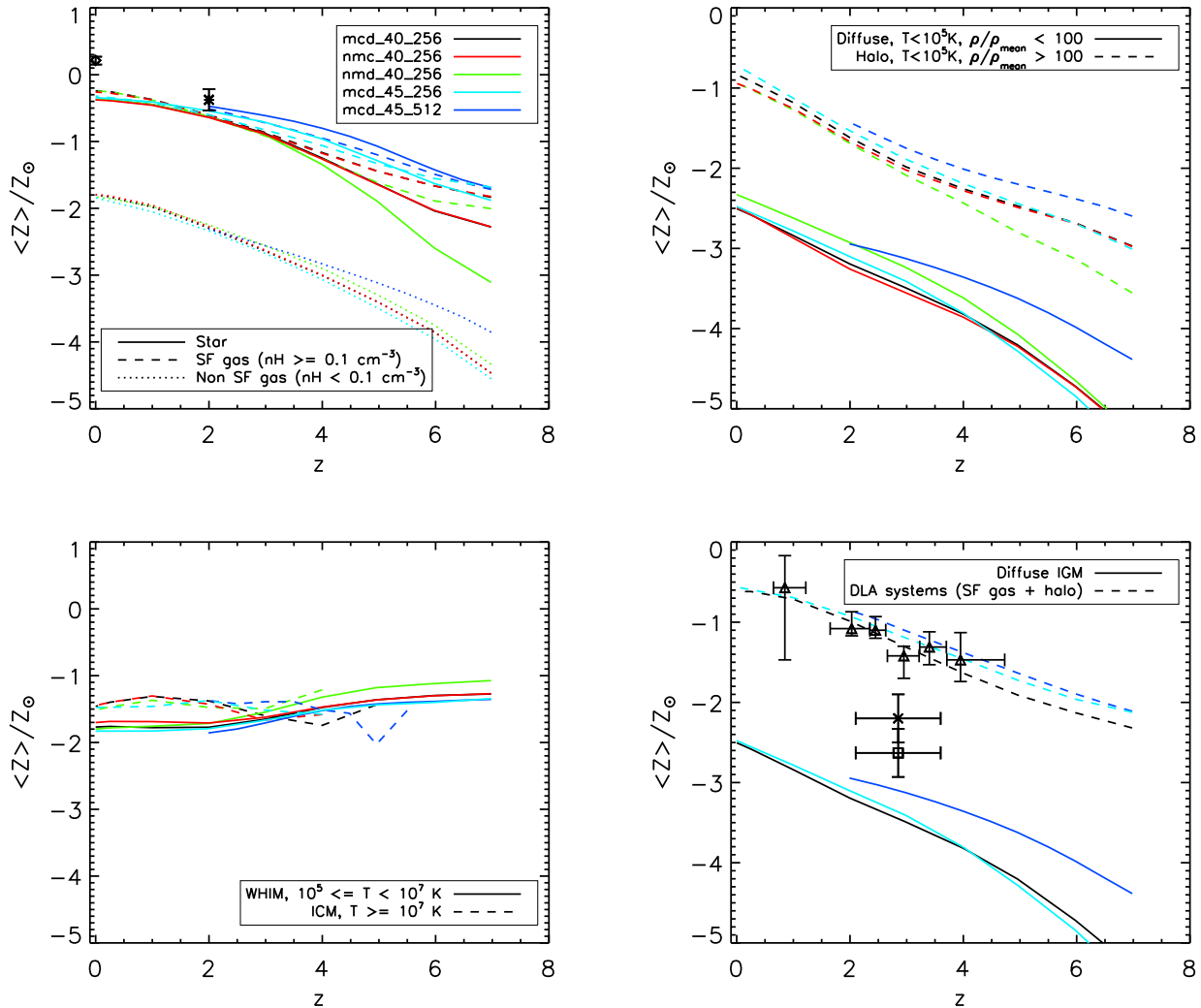


**Figure 6.** The evolution of metallicity in stars and various gas phases described in the text. The same legend as in Figure 5 is used. The solar metallicity is defined as  $Z_{\odot} = 0.0127$ . Observational data: *Diamond*: stellar metallicity at  $z = 0$  (Gallazzi et al. 2008). *Asterisk*: stellar metallicity at  $z = 2$  from Halliday et al. (2008). *Triangles*: the metallicity evolution of DLA and sub-DLA systems from Prochaska et al. (2003). *Cross*: the IGM metallicity traced by O VI from Aguirre et al. (2008); *Square*: the IGM metallicity traced by C IV from Schaye et al. (2003). The observations were scaled to the same solar abundance as the simulations.  $Z_{\odot} = 0.0127$

metallicities are not that high and the cooling times can be very long. The most enriched gas is at the highest densities: star forming gas in galaxies. The metallicity of this gas can be super-solar. The highly enriched gas (near solar metallicities) is all above  $\rho/\rho_{mean} \sim 10^4$ . The metallicity decreases as the wind propagates and mixes moving to lower densities. This steady progression with density can be seen in the hot gas ( $T > 10^5$  K). The WHIM is enriched up to  $10^{-2} Z_{\odot}$  to  $10^{-1} Z_{\odot}$ , while the diffuse IGM following the power-law EOS is barely enriched. The metallicity contours in Figure 7 show that metal enriched IGM is hotter than this diffuse phase.

The metallicity distribution on the phase diagram without metal diffusion in the right panel of Figure 7 is similar, but the metals are less evenly distributed. In particular, more low density material becomes enriched. For example, some gas around  $T \sim 10^4 K$  and  $\rho/\rho_{mean} \sim 0.01$  has metal-

licities up to 0.1 solar. On the other hand, relatively dense, cool halo gas ( $\rho/\rho_{mean} > 100, T < 10^5 K$ ) is less enriched, as shown in the plot that the horizontal strip of lower metallicities extends to higher densities. As discussed in Section 4.3, this is because without metal diffusion, the metals are locked into the original wind material and must travel with it.

The overall trend in metallicity versus density can be seen in Figure 8. The effect of metal diffusion can be clearly seen. The reference run produces a positive, near linear relation between the density and metallicity in logarithmic space for  $\rho/\rho_{mean} > 1$ . The slope is larger for the under-dense gas. The simulation without metal diffusion increases the under-dense gas metallicity by a factor of 3 while it decreases it for halo gas (with overdensities larger than 100). Overall, it gives a shallower slope in the range of  $\log(\rho/\rho_{mean}) = [0, 3]$ . The result from the simulation without metal cool-

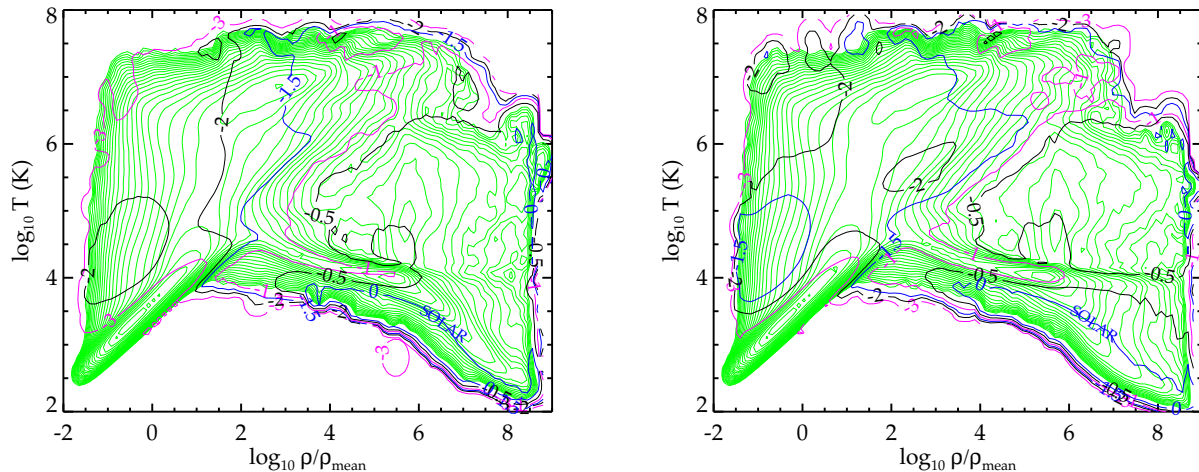


**Figure 7.** Distribution of Gas and Metallicity in the  $\rho$ - $T$  phase diagram of the reference simulation at  $z=0$ . The green contours indicate the gas mass distribution, and the black, magenta and blue contours with labels indicate the metallicities. From low to high, the metallicity labels are  $[\text{Fe}/\text{H}] = -3.0, -2.0, -1.5, -1.0, -0.5$  and  $0.0$ . Solar metallicity is defined as  $Z_{\odot} = 0.0127$ . The left panel is the standard run with metal diffusion and the right panel is without diffusion.

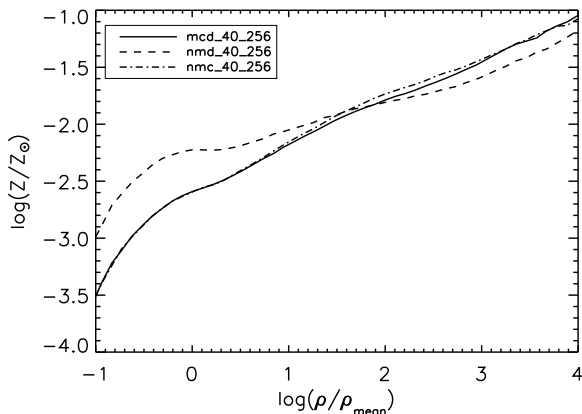


**Figure 8.** The metallicity-density relation at redshift zero for all the simulation runs. The effect of metal diffusion is shown in the excess at the low over density range and the decrease of metallicity in the halo gas.

ing is also plotted, although the effect is relatively small. Observationally, the metallicity-density relation can be inferred from certain metal tracers in the QSO spectra. For example, Schaye et al. (2003) used pixel statistics of C IV and found the carbon abundance follows a log-linear relation with density at the higher redshifts ( $z = 1.8$ - $4.1$ ). These observations may strongly constrain the feedback and wind generation mechanism, but uncertainties due to the shape of the UV background and the ionization states of the metal tracers may change the results substantially, as discussed in Schaye et al. (2003) and Oppenheimer & Davé (2006). We defer detailed comparison of specific species with observations to a following paper.

Figure 9 shows the metal-mass-weighted probability density functions (PDF) over temperature, density and metallicity. Bimodal distributions are seen in the PDF of all

three variables. As seen in the leftmost panel, metal cooling is efficient at WHIM temperatures and shifts a substantial amount of material from the WHIM to lower temperatures and the sharp peak of gas at  $10^4$  K associated with primordial cooling is removed. Without diffusion, super-enriched gas is present which is able to cool to nearly 100 K. Without diffusion, enriched gas is also able to travel to extremely low densities as seen in the second panel.

The impact of metal diffusion is clear in the metallicity distribution (the rightmost panel in Figure 9). With metal diffusion, there is a large increase in material at low metallicities,  $Z < 0.1 Z_{\odot}$ . Without diffusion the metals concentrate in a spike just above  $0.1 Z_{\odot}$  associated with the early distribution of metals from a star formation event. Turbulent mixing spreads the metals from the wind material to the surroundings so that substantially more gas contains metals at low levels. An increase in low metallicity gas was also achieved in Wiersma et al. (2009b) using a local smoothing technique, but a physically motivated diffusion model results in the metals being substantially redistributed in space as seen in the second panel of the figure.

## 6 CHARACTERIZING THE WIND MECHANISM

The primary difference between the simulations presented here and earlier enrichment studies is the mechanism for wind generation. Earlier simulations explicitly added velocity to gas in regions where stars form. Here feedback only added thermal energy and prevented gas cooling according to recipe developed using simulations of isolated Milky Way like disks and dwarf galaxies. We have shown in previous sections that our adiabatic feedback can cause mass loss from galaxies to enrich the IGM. However, since winds are produced dynamically as a result of feedback instead of via a wind recipe, it is helpful to characterize the wind generation mechanisms. In this section, we examine mass loss as a func-

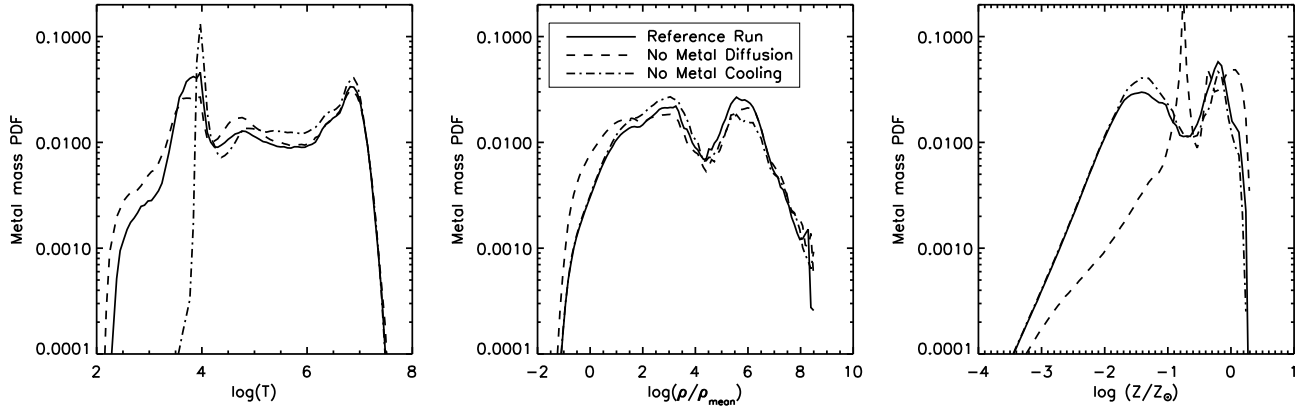


**Figure 9.** The probability density function (PDF) of the metal mass over temperature (left panel), density (center panel) and metallicity (right panel) at  $z=0$ . *Solid lines*: the reference simulation; *Dashed lines*: the simulation without metal cooling; *Dot-dashed lines*: the simulation without metal cooling.

tion of halo mass for our baseline simulations. The purpose is to understand how our current adiabatic feedback generates winds that enrich the IGM. Our results do allow scope for more vigorous feedback. Additional feedback such as explicit superwinds and subgrid AGN models may be included in our future enrichment studies. The results presented here serve as a starting point for further investigations testing more complicated feedback scenarios.

We identified overdense halos using a friends-of-friends (FOF) group finder with linking length  $\epsilon = \frac{1}{5}$  (inter-particle separation  $\sim 30$  kpc) to find material inside regions of overdensity  $\frac{\delta\rho}{\rho} \gtrsim 125$ . We compared the baryon fraction ( $M_{\text{bary}}/M_{\text{tot}}$ ) of material inside the halos (black solid line) as a function of total halo mass at  $z = 0$  with the cosmic mean ( $\Omega_b/\Omega_m$ , dotted line) in the upper panel of Figure 10. The baryon content is low for low mass halos ( $< 10^{10} M_\odot$ ). It increases quickly with mass in the intermediate range, and stays near the cosmic mean beyond  $\sim 10^{11} M_\odot$ . Halos of masses less than  $\sim 10^{11} M_\odot$  contain less than the cosmic mean. Using a lower resolution ( $2 \times 128^3$  particles) run, we ruled out that the decrease below  $\sim 10^{11} M_\odot$  is a resolution effect. This decrease indicates that gas was either prevented from accreting onto those halos, or ejected/stripped from them. Possible mechanisms that cause the mass loss include: 1. Background UV radiation heating the gas and preventing it from accreting onto dwarf galaxies. 2. Tidal stripping during merger events. 3. Winds generated from the stellar feedback mechanism.

We investigated where the “lost” baryons are at the current epoch by pairing each gas particle with its dark matter (DM) partner at the same location in the initial conditions. We identified the gas particles that remain in the IGM (i.e. not belong to any groups) even though their partner dark matter particle has accreted to a halo at  $z=0$ . When plotting any properties of this gas as a function of halo mass, we mean the mass of halos to which the DM partner of the gas is belong. Note that this method only considers the difference between the initial condition and the snapshot at  $z = 0$ , so it does not capture the information in between such as re-accretion of gas after ejection. Hence the result here is used as a qualitative indication of the fate of the “lost” gas. A

more precise description would require track gas particles. According to its temperature, this “lost” gas was categorized as WHIM ( $10^5 \text{K} < T < 10^7 \text{K}$ ) or cooler, diffuse gas ( $T < 10^5 \text{K}$ ). The bottom panel of Figure 10 shows the mass fraction of this gas that is in the form of WHIM (black line with error bars). For comparison, the gas inside halos was also categorized in the same way as warm-hot halo gas and cool halo gas, and the fraction of the halo gas that is in the warm-hot form is shown in the same panel (red line with error bars). Despite of the large error bars, the curves show that gas associated with smaller halos tends to be cooler than that associated with large halos. This is expected because larger halos have larger gravitational potentials and higher virial temperatures.

We investigated the role of stellar feedback and winds in the efficient mass loss by tracing the density history of the “lost” gas up to  $z = 5$  to identify winds. If its highest overdensity,  $\rho(z)_{\text{max}}/\rho_{\text{mean}}$ , was larger than 100, and its current density is less than half of the maximum ( $\rho(z=0) < 0.5 \rho(z)_{\text{max}}$ ), then the gas is considered ejected as wind material. Since the gas density was measured only when snapshots were generated every  $\Delta z = 0.25$ , it is possible that some wind gas was omitted. However, we verified this density method in the non-diffusion simulation, where enriched winds can be identified by the metallicities of the particles. Our density method successfully detects the same material identified by metals. The blue and red lines in the upper panel of Figure 10 indicates fractions of the halo baryons that were expelled as winds, and are currently in the WHIM and cool IGM phase, respectively. We also plotted the stellar mass fractions in the same figure (dashed line).

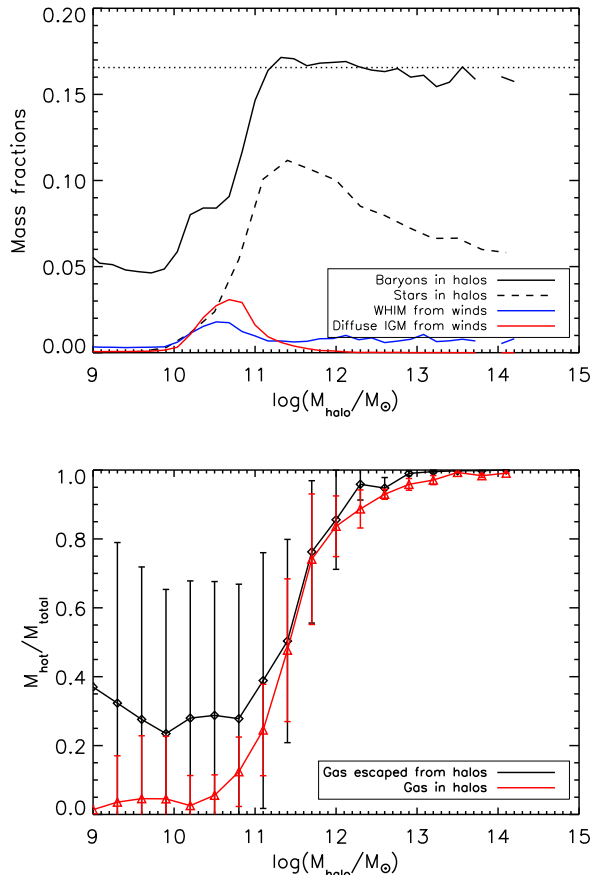
Our results show that baryon loss due to winds is most efficient at intermediate mass ranges,  $10^{10}$  to  $10^{11} M_\odot$ . This is also the range where the stellar fraction increases rapidly, which reflects the correlation between star formation and wind generation. Below  $10^{10} M_\odot$ , baryon fractions of the halos are very low and there are almost no stars and no winds. We traced the accretion history of this gas and found it has never accreted onto any objects. Though higher resolution is necessary to investigate these objects, it is likely

that heating due to the background UV radiation prevents gas accreting onto such halos, since UV heating can bring gas temperature to  $10^4 K - 10^5 K$ , comparable to the virial temperature of dwarf galaxies with mass  $\lesssim 10^{10} M_{sun}$ . Wind fractions start to decrease when  $M > 10^{10.5} M_{\odot}$ . This may be caused by 1. decrease of wind escaping efficiency with increasing halo gravitational potentials; or 2. decrease of star formation efficiency as halo mass increases, as indicated in the decline of stellar fraction in Figure 10. The latter is probably due to the increase of cooling time, as the virial temperature of the halo increases and the cooling rate decreases beyond  $10^6 K$  (ref. Figure 1). For halos with mass  $\gg 10^{12} M_{\odot}$ , virialized gas can have longer cooling time than the dynamical timescale and hence fuel supplies for SF activities can be largely reduced (Rees & Ostriker 1977). It is worth noting that the stellar fraction from our simulation is larger than observations (e.g., Guo et al. 2009) so there is an “overcooling” problem, in which gas in simulations tends to cool too rapidly and form much more stars comparing with observations. It was suggested that feedback from Active Galactic Nuclei (AGN) may alleviate this problem (e.g. McCarthy et al. 2009) especially for galactic groups. However, a discussion of AGN feedback is beyond the scope of this paper, and we use the stellar fraction curve only to indicate SF activities in different mass halos.

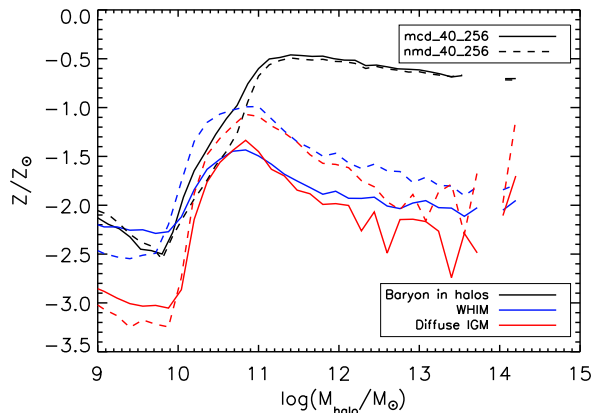
The colored lines in the upper panel of Figure 10 show that the wind material can be in WHIM or cooler IGM phases. Galaxies of all masses larger than  $10^{10} M_{\odot}$  generate winds in the form of WHIM, while only galaxies that in range of  $10^{10} - 10^{12} M_{\odot}$  have cool wind gas. We tracked the temperature history for this cool wind gas and found that about 60 % of it had  $T > 10^5 K$  when it was generated and has subsequently cooled.

Figure 11 shows the metallicity distribution for the baryons within halos, WHIM and diffuse gas as functions of halo mass. Note that here the WHIM and the diffuse gas shown are those that have their paired DM particles inside halos. It is the gas that cannot accrete or has escaped from halos. This is a subset of the total WHIM and diffuse gas described in Section 4. The metallicity for all gas is low for halos with mass  $\lesssim 10^{10} M_{\odot}$ . For the diffuse IGM and the WHIM, it is likely because this gas has never accreted onto galaxies and experienced star formation. For the gas in halos, the metallicity is still low due to low star formation. In the intermediate mass range, the metallicity of the gas in halos increases significantly, because the baryon content of halos increases and the galaxies undergo multiple star formation events and accumulate metals. Consequently, winds are enhanced, increasing the metallicities in the diffuse and WHIM gas outside those halos. The metallicity of baryons in halos saturates above  $\sim 10^{11} M_{\odot}$ , reflecting the decline of SF activity with increasing halo mass. The metallicities of the escaped material (in both the WHIM and cooler IGM phase) decreases, possibly due to the inefficiency of winds leaving more massive objects and the decline of star formation. Note that the amount of diffuse gas is very small in massive objects beyond  $10^{12} M_{\odot}$  so the metallicities have large uncertainties.

The dashed lines in Figure 11 show the metallicities of different gas phases for the non-diffusion run. The effects of metal diffusion are seen in two aspects. First, metal diffusion contaminates the gas that is prevented from accreting due to



**Figure 10. Upper panel:** Distribution of baryon and stellar mass fractions of halos and wind fraction escaped from halos, as a function of total halo mass in the reference run ( $z=0$ ). *Black solid line:* baryon fraction (include gas and stars) in halos. *Dotted line:* the cosmic mean value. *Dashed line:* stellar mass fraction. To indicate how halos of different mass lose gas and the role of stellar feedback and winds, we identify the lost gas by pairing each gas particle with its dark matter neighbour in the initial condition, and finding the ones who have their DM partners within halos but themselves in the IGM. When plotting this gas as a function of halo mass, we mean the mass of halos that its pairing dark matter particle is belong to. The gas found in this method is further split to the WHIM phase ( $10^5 K < T < 10^7 K$ ) and the cooler IGM phase ( $T < 10^5 K$ ). Among this gas, winds were identified by tracing the density history of the gas using  $\rho(z)_{\text{max}}/\rho_{\text{mean}} > 100$  and  $\rho(z=0) < 0.5 \rho(z)_{\text{max}}$ . *Blue solid line:* mass fraction of the halo baryons that escaped as wind and are currently in the WHIM. *Red solid line:* mass fraction of the halo baryons that escaped as wind and are currently in the diffuse IGM. **Lower panel:** For the gas that is currently within or outside of a certain halo, the mass fraction of this gas that is in the warm-hot phase, as a function of the halo mass. *Black curve with error bars:* mass fraction of the gas outside of halos (identified by the partner DM particles) that is in the warm-hot phase (i.e. WHIM). *Red curve with error bars:* mass fraction of halo gas that is in the warm-hot phase.



**Figure 11.** The distribution of metallicities of baryons within halos and different phases of gas that cannot accrete onto or escaped from halos (described in the caption of Figure 10) as a function of total group mass at  $z = 0$ . The solar metallicity used in this plot is  $Z_{\odot} = 0.0127$ .

UV or stripped by tidal forces, as indicated in the increases of the metallicity of the gas associated with low mass halos when metal diffusion is on. Second, metal diffusion allows winds to lose metals along the wind trajectory, therefore significantly decreasing the metallicity in winds, while increasing it in halo gas. This is reflected in the metallicity decrease of the gas outside halos (both the WHIM and the diffuse gas) at mass larger than  $10^{10}M_{\odot}$ , and the increase in the metallicity of the baryons within halos. Without diffusion almost all metals in the unbound gas are locked in wind material (98% of all metals in the WHIM and 99% of all metals in the diffuse IGM). In the full model, including metal diffusion, the numbers decrease to 58% and 80%, respectively.

## 7 SUMMARY AND CONCLUSIONS

We investigated the enrichment of the intergalactic medium with SPH cosmological simulations using an adiabatic stellar feedback model. The simulations incorporated a self-consistent metal cooling model with an ultraviolet (UV) ionizing background along with metal diffusion that models the turbulent mixing in the IGM and the ISM. It was found that the UV background significantly alters the metal cooling rates at all temperatures from 100 K to  $10^9$  K. Above  $10^4$  K it decreases the cooling rate and shifts the cooling peak to higher temperature, while below  $10^4$  K the UV increases the metal cooling rates due to the increase of free electrons.

The simulations produced an SFH broadly consistent with observations to redshift  $z \sim 0.5$ , and a steady cosmic total neutral hydrogen fraction ( $\Omega_{\text{HI}}$ ) that compare relatively well with observations, although possible discrepancies in the observed  $\Omega_{\text{HI}}$  at  $z \sim 2-3$  allow for more vigorous mass-loss. This demonstrates that adiabatic feedback can moderate SF while maintaining a regular supply of H I. The evolution of the mean flux decrement in the Ly- $\alpha$  forest in our simulations is consistent with observations to  $z \sim 3-4$ , if

the magnitude of the UV background is lowered with respect to the Haardt & Madau (2005) rates in CLOUDY.

As the universe evolves, there is a rapid increase in the amount of warm-hot intergalactic medium (WHIM) and a decrease in the cooler diffuse IGM. At  $z=0$ , about 40% of the mass is in WHIM, consistent previous simulations with different methods (Cen & Ostriker 2006; Oppenheimer & Davé 2006). The metal content of the Universe evolves from the largest fraction being in the IGM to the majority residing in star forming gas, to ultimately being locked in stars at the present day. These trends reflect more effective wind escape at high redshift. IGM metals primarily reside in the WHIM, unlike Oppenheimer & Davé (2006) and Davé & Oppenheimer (2007), whose metals largely reside in cool gas, as the wind gas starts cool with kinetic feedback and less likely to be heated up when the wind material is decoupled from the ISM. Our result is however in agreement with Wiersma et al. (2009b) who also used kinetic feedback but with non-decoupled wind models. The mean metallicities of stars, star forming gas, galactic halo gas and the cold diffuse IGM all increase with time, but those of the WHIM and the ICM remain mostly constant with a slight decreasing trend. The metallicity of the WHIM stays between 0.01 to 0.1  $Z_{\odot}$ . The metallicity of the ICM is similar to the WHIM, which is smaller than the observed value, 0.2-0.5  $Z_{\odot}$  (Aguirre & Schaye 2007), possibly due to absent AGN feedback. The metallicity evolution of the gas in galaxies compares well with DLA and sub-DLA observations from Prochaska et al. (2003) and the metallicity of the diffuse IGM at  $z \sim 2.5$  is less than the observations from Schaye et al. (2003) and Aguirre et al. (2008), suggesting higher resolution, or additional mechanisms for enriching the diffuse IGM are probably necessary.

We characterized our galactic mass-loss and wind generation. For the current adiabatic feedback model, winds are most efficient for galaxies in the intermediate mass range of  $10^{10}M_{\odot}$  to about  $10^{11}M_{\odot}$ . Below  $10^{10}M_{\odot}$  gas is likely to be prevented from accreting due to UV heating and remains as low-metallicity gas. Above about  $10^{11}M_{\odot}$  fraction of wind gas decreases, possibly because the wind escape efficiency decreases with increasing halo potentials, or because the decline of star formation activities especially for massive halos. Most winds were hot when generated, but the ones expelled from intermediate mass range galaxies, having temperatures  $\sim 10^5 - 10^6$  K, could cool through metal lines and become diffuse IGM rather than WHIM.

We investigated the effect of metal cooling and diffusion on the SFH, the evolution of  $\Omega_{\text{HI}}$  and the evolution of mass and metals in different phases. For metal diffusion, we further studied its effect in the density-temperature phase diagram at  $z=0$  and the distribution of baryons as function of the galaxy mass. Metals significantly enhance the cooling of the WHIM, allowing the gas to cool and join galactic disks. Metals also enable cooling below  $10^4$  K. Metal cooling decreases the mass and metal fractions of the WHIM while increasing the metals in stars, halos and SF gas and increasing the SFR by 20% and  $\Omega_{\text{HI}}$  by 17% at  $z=0$ . With realistic diffusion included, metals mix between winds and surrounding gas before they leave the galaxies, decreasing the metal content in the WHIM and diffuse IGM but increasing it in the galactic halo and star forming gas. It prevents enriched, hot winds from creating highly-enriched low density

regions, and makes the density-metallicity relation smoother so it follows a nearly log-linear relation in the density range  $\log(\rho/\rho_{mean}) = 0 - 4$ .

We performed two additional simulations with one of which having 8 times more particles, to investigate the convergence of our results and the resolution dependence of our model. Full convergence is not seen in most of our results, however the results from the high resolution run in SFH,  $\Omega_{HI}$  evolution, Ly $\alpha$  decrement evolution are still broadly consistent with observational data, and the differences caused by resolution decrease with redshift. Also, the basic results of metal fraction evolution trend and enrichment efficiency in different gas phases remain unchanged. The impact of resolution can be seen in three aspects. Firstly, with high resolution the amount of neutral gas (H I) and SFR increase, hence the stellar mass fraction and the WHIM mass fraction related to wind activities. The difference is largest at high redshift. Secondly, the metal fraction locked up in stars increases with resolution while decreasing that in the ISM and IGM in general, suggesting a decline in wind efficiency. Thirdly, with high resolution the diffuse IGM and halos have a higher metal fraction at the cost of the WHIM metals.

In future work, we will make a more detailed comparison with metal absorption line observations. We will also examine the detailed behaviour of various wind models and the effect on the immediate environment of galaxies.

## ACKNOWLEDGEMENTS

We would like to thank Robert Wiersma for many useful discussions during the writing of this paper. Andrew Hopkins and Steve Wilkins kindly provided their star formation history data converted for the Kroupa IMF used in this paper. The simulations were performed using the Shared Hierarchical Academic Research Computing Network (SHARCNET) facilities. This work is supported by the National Science and Engineering Research Council (NSERC) of Canada and a Canadian Institute for Theoretical Astrophysics (CITA) National fellowship.

## REFERENCES

- Abel, T., Anninos, P., Zhang, Y., & Norman, M. L. 1997, *New Astronomy*, 2, 181
- Allende Prieto, C., Lambert, D. L., & Asplund, M. 2001, *ApJL*, 556, L63
- Allende Prieto, C., Lambert, D. L., & Asplund, M. 2002, *ApJL*, 573, L137
- Aguirre, A., Schaye, J., Kim, T.-S., Theuns, T., Rauch, M., & Sargent, W. L. W. 2004, *ApJ*, 602, 38
- Aguirre, A., Schaye, J., Hernquist, L., Kay, S., Springel, V., & Theuns, T. 2005, *ApJL*, 620, L13
- Aguirre, A., & Schaye, J. 2007, *EAS Publications Series*, 24, 165
- Aguirre, A., Dow-Hygelund, C., Schaye, J., & Theuns, T. 2008, *ApJ*, 689, 851
- Bernardi, M., et al. 2003, *AJ*, 125, 32
- Bouché, N., Lehnert, M. D., & Péroux, C. 2006, *MNRAS*, 367, L16
- Brooks, A. M., Governato, F., Quinn, T., Brook, C. B., & Wadsley, J. 2009, *ApJ*, 694, 396
- Cen, R., Ostriker, J. P., Prochaska, J. X., & Wolfe, A. M. 2003, *ApJ*, 598, 741
- Cen, R., & Ostriker, J. P. 2006, *ApJ*, 650, 560
- Chevalier, R. A. 1974, *ApJ*, 188, 501
- Choi, J.-H., & Nagamine, K. 2009, *MNRAS*, 393, 1595
- Croft, R. A. C., Weinberg, D. H., Katz, N., & Hernquist, L. 1998, *ApJ*, 495, 44
- Dalla Vecchia, C., & Schaye, J. 2008, *MNRAS*, 387, 1431
- Davé, R., Hellsten, U., Hernquist, L., Katz, N., & Weinberg, D. H. 1998, *ApJ*, 509, 661
- Davé, R., & Oppenheimer, B. D. 2007, *MNRAS*, 374, 427
- Ellison, S. L., Songaila, A., Schaye, J., & Pettini, M. 2000, *AJ*, 120, 1175
- Erb, D. K., Shapley, A. E., Pettini, M., Steidel, C. C., Reddy, N. A., & Adelberger, K. L. 2006, *ApJ*, 644, 813
- Faucher-Giguère, C.-A., Lidz, A., Hernquist, L., & Zaldarriaga, M. 2008, *ApJ*, 688, 85
- Ferland, G. J., Korista, K. T., Verner, D. A., Ferguson, J. W., Kingdon, J. B., & Verner, E. M. 1998, *PASP*, 110, 761
- Ferrara, A., Scannapieco, E., & Bergeron, J. 2005, *ApJL*, 634, L37
- Finoguenov, A., Burkert, A., Boumlhringer, H. 2003, *ApJ*, 594, 136
- Frenk, C., White, S., Bryan, G., Norman, M., Cen, R., Ostriker, G., Couchman, H., Evrard, G., Gnedin, N., Jenkins, A., Pearce, F., Thomas, P., Navarro, H., Owen, J., Villumsen, J., Pen, U.-L., Steinmetz, M., Warren, J., Zurek, w., Yepes, G. & Klypin, A., 1999, *Ap. J.*, 525, 554
- Gallazzi, A., Brinchmann, J., Charlot, S., & White, S. D. M. 2008, *MNRAS*, 383, 1439
- Gnat, O., & Sternberg, A. 2007, *ApJS*, 168, 213
- Governato, F., Willman, B., Mayer, L., Brooks, A., Stinson, G., Valenzuela, O., Wadsley, J., & Quinn, T. 2007, *MNRAS*, 374, 1479
- Grevesse, N., & Sauval, A. J. 1998, *Space Science Reviews*, 85, 161
- Greif, T., Glover, S., Bromm, V., Klessen, R. 2009, *MNRAS*, 392, 1381
- Guo, Q., White, S., Li, C., & Boylan-Kolchin, M. 2009, *arXiv:0909.4305*
- Haardt F., Madau P. 2005, *unpublished*
- Halliday, C., et al. 2008, *A&A*, 479, 417
- Heckman, T. M., Armus, L., & Miley, G. K. 1990, *ApJS*, 74, 833
- Heckman, T. M. 2001, *Gas and Galaxy Evolution*, 240, 345
- Holweger, H. 2001, *Joint SOHO/ACE workshop "Solar and Galactic Composition"*, 598, 23
- Hopkins, A. M. 2004, *ApJ*, 615, 209
- Hui, L., & Gnedin, N. Y. 1997, *MNRAS*, 292, 27
- Jimenez, R., Flynn, C., MacDonald, J., & Gibson, B. K. 2003, *Science*, 299, 1552
- Katz, N., Weinberg, D. H., & Hernquist, L. 1996, *ApJS*, 105, 19
- Kay, S. T., Pearce, F. R., Frenk, C. S., & Jenkins, A. 2002, *MNRAS*, 330, 113
- Kennicutt, R. C., Jr., Tamblyn, P., & Congdon, C. E. 1994, *ApJ*, 435, 22
- Kennicutt, R. C., Jr. 1998, *ApJ*, 498, 541
- Kirkman, D., Tytler, D., Lubin, D., & Charlton, J. 2007,

- MNRAS, 376, 1227
- Komatsu, E., et al. 2009, ApJS, 180, 330
- Kroupa, P., Tout, C. A., & Gilmore, G. 1993, MNRAS, 262, 545
- Lah, P., et al. 2007, MNRAS, 376, 1357
- Mac Low, M.-M., & Ferrara, A. 1999, ApJ, 513, 142
- Mac Low, M.-M., & Klessen, R. S. 2004, Reviews of Modern Physics, 76, 125
- Mashchenko, S., Wadsley, J., & Couchman, H. M. P. 2008, Science, 319, 174
- McCarthy, I. G., et al. 2009, arXiv:0911.2641
- McKee, C. F., & Ostriker, J. P. 1977, ApJ, 218, 148
- Murray, N., Quataert, E., & Thompson, T. A. 2005, ApJ, 618, 569
- Nagamine, K., Springel, V., & Hernquist, L. 2004, MNRAS, 348, 421
- Navarro, J. F., & White, S. D. M. 1993, MNRAS, 265, 271
- Nagamine, K., Springel, V., & Hernquist, L. 2004, MNRAS, 348, 435
- Navarro, J. F., & Steinmetz, M. 1997, ApJ, 478, 13
- Oppenheimer, B. D., & Davé, R. 2006, MNRAS, 373, 1265
- Oppenheimer, B. D., & Davé, R. 2009, MNRAS, 395, 1875
- Pettini, M., Shapley, A. E., Steidel, C. C., Cuby, J.-G., Dickinson, M., Moorwood, A. F. M., Adelberger, K. L., & Giavalisco, M. 2001, ApJ, 554, 981
- Pettini, M., Madau, P., Bolte, M., Prochaska, J. X., Ellison, S. L., & Fan, X. 2003, ApJ, 594, 695
- Pontzen, A., et al. 2008, MNRAS, 390, 1349
- Prochaska, J. X., Gawiser, E., Wolfe, A. M., Castro, S., & Djorgovski, S. G. 2003, ApJL, 595, L9
- Prochaska, J. X., Herbert-Fort, S., & Wolfe, A. M. 2005, ApJ, 635, 123
- Prochaska, J. X., & Wolfe, A. M. 2009, ApJ, 696, 1543
- Rao, S. M., Turnshek, D. A., & Nestor, D. B. 2006, ApJ, 636, 610
- Rees, M. J., & Ostriker, J. P. 1977, MNRAS, 179, 541
- Raiteri, C. M., Villata, M., & Navarro, J. F. 1996, A&A, 315, 105
- Schaye, J., Rauch, M., Sargent, W. L. W., & Kim, T.-S. 2000, ApJL, 541, L1
- Schaye, J., Aguirre, A., Kim, T.-S., Theuns, T., Rauch, M., & Sargent, W. L. W. 2003, ApJ, 596, 768
- Schaye, J., Carswell, R. F., & Kim, T.-S. 2007, MNRAS, 379, 1169
- Schaye, J., et al. 2010, MNRAS, 402, 1536
- Silich, S., & Tenorio-Tagle, G. 2001, ApJ, 552, 91
- Simcoe, R. A., Sargent, W. L. W., & Rauch, M. 2004, ApJ, 606, 92
- Simcoe, R. A. 2006, AJ, 653, 977
- Smith, B., Sigurdsson, S., & Abel, T. 2008, MNRAS, 385, 1443
- Songaila, A., & Cowie, L. L. 1996, AJ, 112, 335
- Sommer-Larsen, J., Götz, M., & Portinari, L. 2003, ApJ, 596, 47
- Smagorinsky, J., 1963, Monthly Weather Rev., 91, 3, 99
- Springel, V., & Hernquist, L. 2003, MNRAS, 339, 312
- Stinson, G., Seth, A., Katz, N., Wadsley, J., Governato, F., & Quinn, T. 2006, MNRAS, 373, 1074
- Strickland, D. K., & Stevens, I. R. 2000, MNRAS, 314, 511
- Sutherland, R. S., & Dopita, M. A. 1993, ApJS, 88, 253
- Thacker, R. J., & Couchman, H. M. P. 2000, ApJ, 545, 728
- Theuns, T., Viel, M., Kay, S., Schaye, J., Carswell, R. F., & Tzanavaris, P. 2002, ApJL, 578, L5
- Thielemann, F.-K., Nomoto, K., & Yokoi, K. 1986, A&A, 158, 17
- Tremonti, C. A., et al. 2004, ApJ, 613, 898
- Veilleux, S., Cecil, G., & Bland-Hawthorn, J. 2005, ARA&A, 43, 769
- Wadsley, J. W., Stadel, J., & Quinn, T. 2004, New Astronomy, 9, 137
- Wadsley, J., Veeravalli, G., & Couchman, H., 2008, MNRAS, 387, 427
- Weidemann, V. 1987, A&A, 188, 74
- Wiersma, R. P. C., Schaye, J., & Smith, B. D. 2009, MNRAS, 393, 99
- Wiersma, R. P. C., Schaye, J., Theuns, T., Dalla Vecchia, C., & Tornatore, L. 2009, arXiv:0902.1535
- Wilkins, S. M., Trentham, N., & Hopkins, A. M. 2008, MNRAS, 385, 687
- Williams, R. J. R., & Dyson, J. E. 2002, MNRAS, 333, 1
- Wolfe, A. M., Gawiser, E., & Prochaska, J. X. 2005, ARA&A, 43, 861
- Wolfire, M. G., McKee, C. F., Hollenbach, D., & Tielens, A. G. G. M. 2003, ApJ, 587, 278
- Woosley, S. E., & Weaver, T. A. 1995, ApJS, 101, 181
- Zwaan, M. A., Meyer, M. J., Staveley-Smith, L., & Webster, R. L. 2005, MNRAS, 359, L30